AALTO UNIVERSITY
School of Electrical Engineering
Department of Radio Science and Engineering

Kalle Piiroinen

DESIGN AND MEASUREMENT OF A FLAT DIELECTRIC LENS ANTENNA FOR BEAM STEERING

The thesis was submitted in partial fulfilment for the degree of Master of Science in Espoo, 25.9.2013

Supervisor

Professor Antti Räisänen

Instructor

Juha Ala-Laurinaho, D.Sc. (Tech.)

Aalto University
School of Electrical
Engineering

Abstract of the Master's Thesis

Author: Kalle Piiroinen	
Title of the Thesis: Design and measurement of a flat dielectric lens antenna for beam steering	
Date: 25.9.2013	**Number of pages:** 9 + 59
Department: Department of Radio Science and Engineering	
Professorship: Radio Engineering, S-26	
Supervisor: Professor Antti Räisänen	
Instructor: Juha Ala-Laurinaho, D.Sc. (Tech.)	
Language: English	

In this thesis, flat hemi-elliptic dielectric lens antennas are studied at millimeter wavelengths. The used lens materials are teflon and a commercial plastic called preperm450, developed specifically for high frequency antenna applications. The main focus of this work is in the beam steering properties of the antennas. Proposed antenna structure is suitable for, e.g., automotive radar applications.

Two different lens configurations are studied, one based on a dielectric slab waveguide and another based on a parallel plate waveguide. The design process for both antenna types is presented in detail and the antenna structures are simulated using commercial simulation software. Both antennas are fed with a WR-10 waveguide.

Four prototype antennas (one of each type, and of both materials) are manufactured using water jet cutting. Manufactured antennas are measured using a planar near-field scanner and the results are compared with the simulated results. In the measurements and simulations beam steering is realized by changing the positioning of the waveguide feed.

The measurement results follow the simulation results to a large extent and confirm the suitability of the proposed antenna structure for beam steering applications at millimeter wavelengths. The low relative permittivity of teflon lenses limits the maximum beam steering angle, especially with the dielectric slab extended lens. Preperm450 proves to be a viable option when choosing materials for dielectric lenses and beam steering angles up to 15° can be achieved with small feed offsets.

Key words: beam steering, hemi-elliptical, integrated lens antenna, dielectric slab waveguide, parallel-plate waveguide

Aalto-yliopisto
Sähkötekniikan
korkeakoulu

Diplomityön tiivistelmä

Tekijä: Kalle Piiroinen

Työn nimi: Keilanohjaukseen soveltuvan litteän dielektrisen linssiantennin suunnittelu ja mittaus

Päiväys: 25.9.2013 | **Sivumäärä:** 9 + 59

Osasto: Radiotieteen ja -tekniikan laitos

Professuuri: Radiotekniikka, S-26

Valvoja: Professori Antti Räisänen

Ohjaaja: TkT Juha Ala-Laurinaho

Kieli: Englanti

Teknologian nopea kehittyminen on mahdollistanut millimetriaaltoalueen käyttöönoton mm. tiedonsiirrossa ja tutkasovelluksissa, mikä on myös kasvattanut mielenkiintoa dielektrisiä linssiantenneja kohtaan. Millimetriaaltoalueella linssiantennien fyysiset mitat ovat pieniä, mikä mahdollistaa niiden käytön myös liikuteltavissa sovelluksissa.

Tässä diplomityössä tutkitaan litteitä dielektrisiä linssiantenneja E-taajuuskaistan (71 – 86 GHz) sovelluksiin. Tutkimuksen suurin mielenkiinnon kohde on antennien keilanohjausominaisuudet, joita tutkitaan syöttöpistettä muuttamalla. Litteä linssiantenni tarjoaa viuhkamaisen keilan, jota keilaamalla voidaan kattaa laajoja alueita. Tämä mahdollistaa tutkitun antennityypin käytön esimerkiksi autotutkissa.

Työssä käsitellään kahdenlaisia antennikonfiguraatioita. Ensimmäinen koostuu linssistä, syöttöantennista ja tukirakenteista, kun taas jälkimmäisessä linssi on suljettu kahden metallilevyn väliin. Käytetyt linssimateriaalit ovat teflon ja preperm450, joka on varta vasten korkean taajuuden antennisovelluksiin suunniteltu kaupallinen muovimateriaali.

Linssien suunnitteluprosessi on kuvailtu yksityiskohtaisesti ja fyysiset mitat optimoitiin tietokoneohjelmiston avulla. Suunnitelluista antenneista valmistettiin neljä erilaista antenniprototyyppiä, jotka mitattiin lähikenttä-skannerin avulla.

Mittaustulosten ja tietokonesimulaatioiden vertailu osoittaa, että antenniprototyyppien mitattu toiminta mukailee hyvin simuloitujen linssien toimintaa. Teflonlinsseillä keilanohjausta rajoittaa matala suhteellinen permittiivisyys, mutta preperm450 osoittautuu hyvin soveltuvaksi dielektristen linssien valmistusmateriaaliksi.

Avainsanat: keilanohjaus, hemielliptinen, integroitu linssiantenni, dielektrinen liuskajohto, levyaaltoputki

Preface

This Master's thesis is carried in the Millimetre wave and THz techniques research group in the Department of Radio Science and Engineering (RAD) of the Aalto University School of Electrical Engineering between February and September 2013. The measurements for this research were conducted at RAD in MilliLab, which is a joint institute between the Technical Research Centre of Finland (VTT) and the Aalto University, and an external laboratory of the European Space Agency (ESA). This work if partially funded by the Academy of Finland through their Centre of Excellence program SMARAD and by TEKES through BEAMS project. Premix Corporation is acknowledged for providing lens materials for this study.

I'd like to thank Professor Antti Räisänen for providing me with the opportunity to work here at the Department of Radio Science and Engineering, and for supervising this thesis. I'd also like to thank my instructor Juha Ala-Laurinaho, D.Sc. (Tech.) for his expert guidance throughout this process. I'm especially grateful to Aki Karttunen, D.Sc. (Tech.) for his opinions, guidance, observations, and instructions during this, as well as all the previous projects. Lastly, I'd like to express my gratitude to my friends and family who made the past eight months so much easier.

In Otaniemi, Espoo, 19.9.2013

Kalle Piiroinen

Contents

List of abbreviations

2-D	Two-dimensional
3-D	Three-dimensional
AUT	Antenna under test
CATR	Compact antenna test range
DSW	Dielectric slab waveguide
DUT	Device under test
EM	Electromagnetic
FEA	Finite element analysis
FEM	Finite element method
FSLL	First side-lobe level
HFSS	High frequency structure simulator
HPBW	Half-power beamwidth
MEMS	Micro-electro-mechanical systems
PPW	Parallel plate waveguide
RF	Radio frequency
SLL	Side-lobe level
TE	Transverse electric
TM	Transverse magnetic
XP	Cross-polarization

List of symbols

a	Minor axis of an ellipse
A	Constant
b	Major axis of an ellipse
B	Constant
c	Focal point of an ellipse, speed of light
C	Constant
c_0	Speed of light in a vacuum
d	Half of lens thickness
D	Antenna dimension, Directivity, constant
e	Eccentricity, exponential function
E	Amplitude of electric field
$\bar{E}$	Electric field
f	Frequency
f_c	Cut-off frequency
$f(x)$	Arbitrary function of x
G	Gain
H	Amplitude of magnetic field
$\bar{H}$	Magnetic field
k_0	Free-space propagation constant
k_x	Propagation constant into the x-direction
L	Dielectric extension length
m	Order of wave mode, index
n	Index of refraction, order of wave mode
n_1	Index of refraction of the cladding
n_2	Index of refraction of the dielectric medium
n_{eff}	Effective index of refraction
r	Distance, spherical coordinate
R	Radius
t	Time
$\tan\delta$	Dielectric loss tangent
$\tan\delta_m$	Magnetic loss tangent
x	Cartesian coordinate
y	Cartesian coordinate
z	Cartesian coordinate
α	Attenuation constant
β	Phase constant
ΔL	Correction in the dielectric extension length
ε	Permittivity
ε_0	Permittivity of free space

ε_r	Relative permittivity
Θ	Spherical coordinate
Θ_0	Angle of incidence
Θ_1	Angle of reflection, angle of refraction
Θ_{3dB}	Half-power beamwidth in E-plane
Θ_c	Critical angle
λ	Wavelength
λ_0	Wavelength in free space
μ	Permeability
μ_0	Permeability of free space
μ_r	Relative permeability
ϕ_{3dB}	Half-power beamwidth in H-plane
ϕ	Spherical coordinate
ω	Angular frequency

1. Introduction

The interest towards dielectric lens antennas has been increasing continuously during recent years due to the advancement of technologies operating at the mm-wave frequencies (30 − 300 GHz). At these frequencies the physical size and weight of the antennas become relatively small, hence making dielectric lens antennas an attractive antenna solution, especially for mobile applications. In addition, dielectric lens antennas traditionally offer a high gain at a low cost, and a shapeable radiation pattern. [1 − 3]

One reason for the increased interest towards dielectric lens antennas is the growing demand for devices with beam steering capability, i.e., changing the direction of the main beam of the radiation pattern [4]. Typical applications exploiting steerable beams include radar [5], imaging tools [6], free-space optical communication systems [7].

Beam steering can be realized either mechanically or electrically. Mechanical beam steering is typically implemented with reflector antennas which are rotated in order to change the direction of the main lobe, whereas electrical beam steering is realized by modifying the feed antenna. Recently, electrical beam steering has become more attractive due to the small size and light weight of the devices at mm-wave frequencies. Electrical beam steering can be realized in several ways, including use of phased arrays [8], phase shifters based on micro-electro-mechanical systems (MEMS) [9], and dielectric lenses with feed antenna array on focal plane. [10, 11]

A solution for beam steering in one dimension at E-band (71 − 86 GHz) using a planar dielectric lens antenna fed with an open-ended waveguide is presented in this thesis. A fan shaped beam makes the proposed antenna structure especially desirable for scanning radars, e.g., automotive radar, while the relatively small size of the antenna makes it suitable for portable devices.

This thesis is structured as follows: Chapter 2 offers a short overview of dielectric lens antennas and their structure. Chapter 3 concentrates on the underlying theory behind flat dielectric slab waveguide

extended lens antennas, including an elaborate and complete field solutions starting from the general wave equation. In Chapter 4 the design process of the lens antennas is presented and physical dimensions are calculated. Chapter 5 describes the computer simulation process and optimization procedure, as well as discusses the importance of microwave absorbers surrounding the antenna. Chapter 6 concentrates on the other studied lens configurations. Theory, design process, and simulation of all the lenses are covered. Antenna measurements and the manufacturing of the prototype antennas are discussed in Chapter 7. Measurement results are presented and discussed in Chapter 8, followed by concluding remarks in Chapter 9.

2. Dielectric lens antennas

Dielectric lens antennas are fairly simple structures consisting of two main parts: the feed and the lens. The feed can be positioned either behind the lens, for example in the case of a cylindrical lens antenna (Figure 1a), or attached to the dielectric material, like in integrated lens antennas (Figure 1b). This chapter concentrates on integrated lens antennas.

The feed can be essentially any kind of radiator, although in practice the vast majority of the used feeding mechanisms are microstrip patch antennas, horn antennas, and open-ended waveguides. Lenses are typically used to convert a spherical wave into a plane wave, and to increase directivity compared to the plain feed antenna by collimating the radiated power into a desired direction. In some cases, the collimation is done only in one dimension resulting in wider, fan-shaped beams which can be used for scanning purposes. [12]
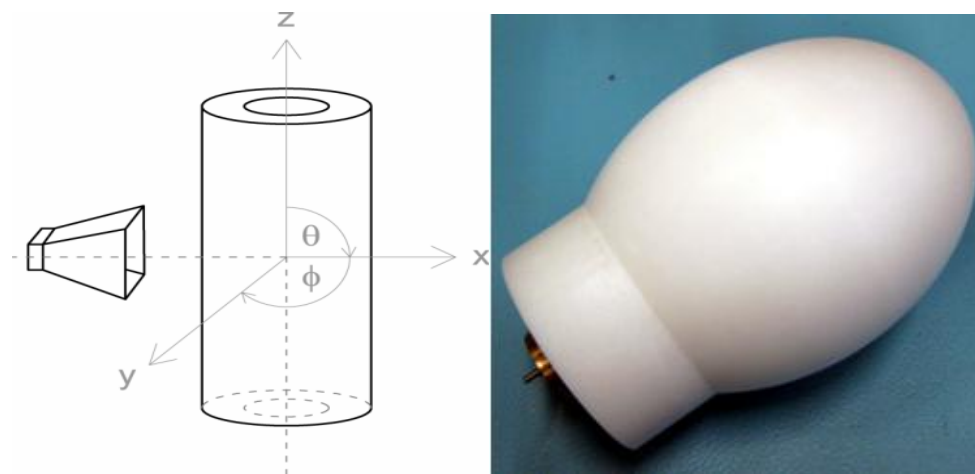

Figure 1: a) Cylindrical dielectric lens antenna [12] and b) Integrated dielectric lens antenna [13].

Microstrip antennas are low-profile, low-cost, and easy to manufacture, hence offering a viable feeding option for integrated lens antennas. Microstrip patch antennas can be designed specifically for a certain frequency which enables simultaneous optimization of the lens and the feed. The most significant disadvantages of patch antennas are the narrow bandwidth and losses that increase with

frequency, which make the microstrip antennas less desirable at higher frequencies. If the broadband characteristic of the lens antennas needs to be exploited, horn antennas or open-ended waveguides can be used as feeding mechanisms. Both are easy to implement and excite, but horn antennas offer a higher gain and provide better optimization possibilities. The biggest downside in both cases is the bulky nature which limits the integrability. [12, 14]

Large number of studies has been published regarding integrated dielectric lens antennas. Traditionally, lenses are symmetrical and three-dimensional (3-D) with varying shapes, such as hemispherical (e.g., [15 − 17]) or ellipsoidal (e.g., [1, 18]). Especially hemispherical lenses are often designed based on Lüneburg's principle. The idea is that the relative permittivity changes from the center to the surface, starting from 2.0 in the middle and following equation

$$\varepsilon_r = 2 - \left(\frac{r}{R}\right)^2, \tag{2.1}$$

where R is the radius of the lens, and r is the radial distance from the center. An ideal Lüneburg lens is a complete sphere but the principle can be expanded to hemispherical lenses. In practice, manufacturing of an ideal Lüneburg lens is not feasible but it can be approximated by using several layers of materials with different values of relative permittivity. [19, 20]

Recent studies have shown that in addition to aforementioned symmetrically shaped lenses, different optimization methods, such as genetic algorithms and particle swarm optimization, can be used to design lenses of arbitrary shapes. Lens shape optimization allows the designer to synthesize lenses based on the desired radiation pattern. The design goal can be, for example, a maximum directivity or a pattern with a certain characteristic, e.g., a flat top. Optimization methods have been applied in lens design in, e.g., [21 − 24].

Lenses with flat, effectively two-dimensional (2-D) structures have also been studied (e.g., [25, 26]), although not as extensively as three-dimensional ones. Flat lenses offer some advantages compared to 3-D lenses, most meaningful being the small physical size, which can be extremely beneficial in mobile applications. With 2-D lenses, the thickness of the lens is an important factor in the design process, and the field analysis is performed in a similar manner as in the design of dielectric slab waveguides. This analysis is covered in detail in Chapter 3.

3. Dielectric slab waveguide

The field solutions within a flat lens can be found by studying a dielectric slab waveguide (DSW), which consists of a dielectric slab surrounded by another dielectric material or air. Fields in the DSW can be solved in a similar manner as in a traditional dielectric rectangular waveguide. The only difference is that some permittivity corrections are required due to the fact that the fields propagate partly as surface waves. Permittivity corrections decrease the effective relative permittivity in comparison to the relative permittivity of the DSW material, hence increase the propagation constant within the waveguide. Section 3.1 gives a detailed description of the DSW while Section 3.2 concentrates on the fields within the DSW, starting from the general wave equation. In Section 3.3 cut-off frequency for different wave modes is derived.

3.1.   Geometry of the dielectric slab waveguide

The geometry of a DSW with a thickness of $2d$ is presented in Figure 2. For the purpose of the analysis, the width and length of the slab are considered to be large compared to the thickness of the slab. Propagation of the wave depends heavily on the angle of incidence θ_0. If the angle is too large, θ_1 becomes too small and the ray does not reflect from the inner wall of the waveguide. The minimum value of θ_1 required for a total internal reflection to occur is called the critical angle θ_c. If $\theta_1 > \theta_c$ the ray will reflect and continue to propagate inside the waveguide, whereas if $\theta_1 < \theta_c$ the ray will partly refract into the cladding. A condition for θ_c can be determined based on Snell's law.
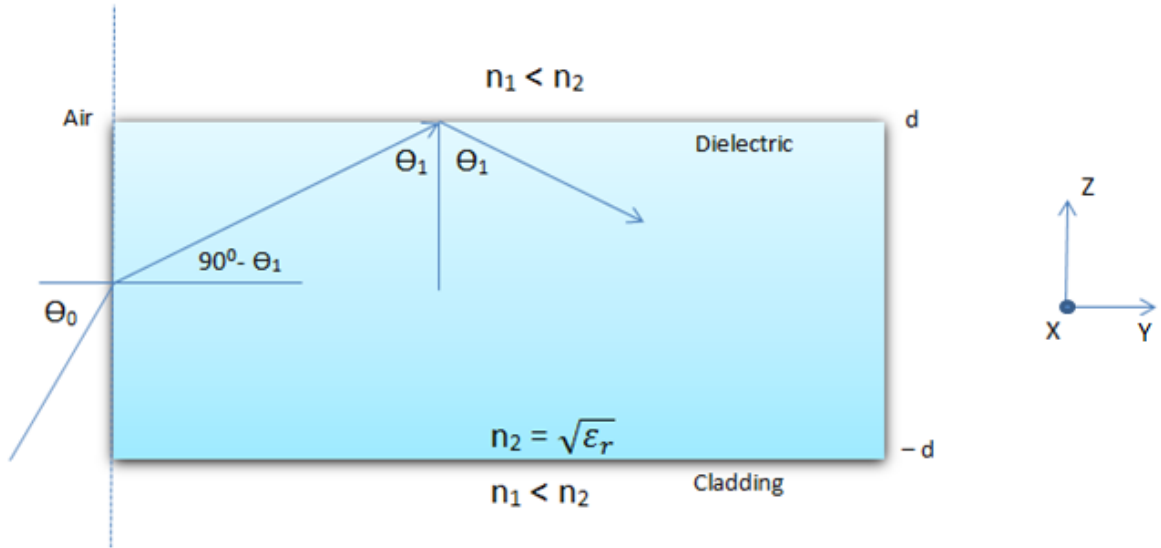
Figure 2: Geometry of a dielectric slab waveguide. [27]

Snell's law states that the relation between the angle of incidence and the angle of refraction is equal to the inverse of the ratio of the indices of refraction [28]. For the critical angle, Snell's law can be written as

$$\sin \theta_c = \frac{n_2}{n_1} \qquad (3.1)$$

and the phase constant (into the direction of y-axis in Figure 2) in the slab can be written as

$$\beta = k_0 n_2 \sin \theta_1. \qquad (3.2)$$

Based on these equations and the condition for the total internal reflection, limits for β can be derived as

$$k_0 n_1 < \beta < k_0 n_2. \qquad (3.3)$$

The free-space wavenumber k_0 and the phase constant β can be used to define the effective index of refraction of the DSW as

$$n_{eff} \equiv \frac{\beta}{k_0}, \qquad (3.4)$$

which can be inserted into (3.3) resulting in

$$n_1 < n_{eff} < n_2. \qquad (3.5)$$

3.2.   Fields in the dielectric slab waveguide

Extensive treatments regarding the field solutions in the DSW can be found from the literature. This section is largely based on the theory provided in [27, 29 – 32].

General solutions for the electric and magnetic fields in a homogenous waveguide are known and can be written in time-harmonic form as

$$\bar{E}(x,y) = \bar{E}_m(x)e^{-j\beta y} \tag{3.6}$$

$$\bar{H}(x,y) = \bar{H}_m(x)e^{-j\beta y}, \tag{3.7}$$

where subscript m refers to the wave mode in question. Inserting (3.6) into the general homogenous wave equation

$$\nabla^2 \bar{E} + \omega^2 \mu \varepsilon \bar{E} = 0 \tag{3.8}$$

results in

$$\frac{\partial^2}{\partial x^2}\bar{E} + (k_0^2 n^2 - \beta)\bar{E} = 0, \tag{3.9}$$

where μ is the permeability, ε is the permittivity, and n is the index of refraction of the corresponding domain. The angular frequency ω is given by

$$\omega = \frac{2\pi f}{c}, \tag{3.10}$$

where f is the operating frequency and c is the speed of light

$$c = \frac{1}{\sqrt{\varepsilon \mu}}. \tag{3.11}$$

Equation (3.9) is a constant coefficient equation which has a well-known general solution of an exponential form. The solution is different for each part of the waveguide. Within the dielectric ($|x| < d$) the solution is

$$E_m(x) = Ae^{jk_x x} + Be^{-jk_x x}, \tag{3.12}$$

where k_x is the propagation coefficient into the direction of x-axis, given by

$$k_x = \sqrt{k_0^2 n_2^2 - \beta^2}. \tag{3.13}$$

For the fields in the cladding ($|x| > d$) the solution is

$$E_m(x) = Ce^{jgx} + De^{-jgx}, \tag{3.14}$$

where g can be written as

$$g = \sqrt{k_0^2 n_1^2 - \beta^2}. \tag{3.15}$$

According to (3.3) g is imaginary, so (3.14) can be written as

$$E_m(x) = Ce^{\alpha x} + De^{-\alpha x}, \tag{3.16}$$

where α is the attenuation coefficient

$$\alpha = \sqrt{\beta^2 - k_0^2 n_1^2}. \tag{3.17}$$

For a wave to be guided, the fields need to decay (i.e., the argument of the exponent function needs to be negative) in the cladding, which means that only one of the components of (3.16) is present at a time.

The total electric field can be obtained by inserting the equations for E_m into (3.6):

$$\bar{E}(x,y) = \begin{cases} \left(Ae^{jk_x x} + Be^{-jk_x x}\right)e^{-j\beta y} & |x| < d \\ Ce^{-\alpha x - j\beta y} & x > d \\ De^{\alpha x - j\beta y} & x < -d. \end{cases} \tag{3.18}$$

Equations for the magnetic field can be derived from Faraday's law

$$\nabla \times \bar{E} = -j\omega\mu\bar{H}. \tag{3.19}$$

In order to find the values of the unknown constants A, B, C, D and β, boundary conditions have to be applied at the interface of the dielectric medium and the cladding ($x = \pm d$). Since the boundary conditions depend on the polarization of the wave, TE (transverse electric) and TM (transverse magnetic) polarizations need to be analyzed independently.

3.2.1. TE modes

In the case of TE polarization, the electric field is normal to the direction of propagation, i.e., the electric field has only a *y*-component. In this case the magnetic field has both *x*- and *z*-components.

The boundary conditions state that the tangential components of the electric and magnetic fields are continuous over the dielectric – cladding interface. Taking into account the orientation of the electric field, Equation (3.19) results in

$$\bar{H}(x) = -\frac{1}{j\omega\mu}\left(\frac{\partial E_y}{\partial x}\right)$$
(3.20)

which means that the magnetic field is continuous if the derivative of the electric field is continuous across the $x = \pm d$ boundaries.

The boundary conditions for the electric field can be written as

$$A\sin(k_x d) + B\cos(k_x d) = Ce^{-\alpha d}, \qquad x = d$$
(3.21)

$$-A\sin(k_x d) + B\cos(k_x d) = De^{-\alpha d}, \qquad x = -d$$
(3.22)

and for the derivative of the electric field as

$$k_x A\cos(k_x d) - k_x B\sin(k_x d) = -\alpha Ce^{-\alpha d}, \qquad x = d$$
(3.23)

$$k_x A\cos(k_x d) + k_x B\sin(k_x d) = \alpha De^{-\alpha d}, \qquad x = -d .$$
(3.24)

These equations can be re-ordered to produce

$$\begin{cases} 2A\sin(k_x d) = (C - D)e^{-\alpha d} \\ 2k_x A\cos(k_x d) = -\alpha(C - D)e^{-\alpha d} \\ 2B\cos(k_x d) = (C + D)e^{-\alpha d} \\ 2k_x B\sin(k_x d) = \alpha(C + D)e^{-\alpha d}. \end{cases}$$
(3.25)

3.2.2. Symmetric and anti-symmetric modes

The symmetric geometry and homogeneous index of refraction mean that the fields inside the waveguide will be either symmetric (even) or anti-symmetric (odd) with respect to the *yz*-plane. This means that the solutions for TE and TM modes need to be divided further into symmetric and anti-symmetric cases. To illustrate this behavior, an arbitrary function *f(x)* can be used as an example: by

definition, *f* is even if *f(x)* = *f(-x)* and odd if *f(x)* = *-f(-x)* [33]. These definitions can be applied to (3.18) which will help in solving the unknown parameters *A, B, C,* and *D.*

Starting with the fields at *x* = ± *d,* for even modes the result is

$$\bar{E}(x=d) = \bar{E}(x=-d) \;\Rightarrow\; Ce^{-\alpha d - j\beta z} = De^{-\alpha d - j\beta z} \;\Rightarrow\; C = D. \tag{3.26}$$

For odd modes the analysis is essentially identical but results in *C = −D.*

Within the waveguide, for even modes

$$E(x) = E(-x) \Rightarrow A\sin(k_x x) + B\cos(k_x x) = A\sin(-k_x x) + B\cos(-k_x x)$$
$$\Rightarrow 2A\sin(k_x x) = 0 \Rightarrow A = 0 \tag{3.27}$$

and for odd modes

$$E(x) = -E(-x) \Rightarrow A\sin(k_x x) + B\cos(k_x x) = -A\sin(-k_x x) - B\cos(-k_x x)$$
$$\Rightarrow 2B\cos(k_x x) = 0 \Rightarrow B = 0. \tag{3.28}$$

Now these results can be applied to the boundary conditions (3.25). For even modes this results in

$$\begin{cases} 2B\cos(k_x d) = 2Ce^{-\alpha d} \\ 2k_x B\sin(k_x d) = 2\alpha Ce^{-\alpha d} \end{cases} \tag{3.29}$$

which can be simplified to

$$k_x \tan(k_x d) = \alpha. \tag{3.30}$$

Similarly for odd modes:

$$\begin{cases} 2A\sin(k_x d) = 2Ce^{-\alpha d} \\ 2k_x A\cos(k_x d) = -2\alpha Ce^{-\alpha d} \end{cases} \tag{3.31}$$

which results in

$$-k_x \cot(k_x d) = \alpha. \tag{3.32}$$

Combining these results with (3.13) and (3.17) results in

$$\tan^2\left(k_0 d\sqrt{n_1^2 - n_{eff}^2}\right) = -\frac{1 - n_{eff}^2}{n_1^2 - n_{eff}^2}, \quad \text{for even modes}$$

$$\tag{3.33}$$

$$\cot^2\left(k_0 d\sqrt{n_1^2 - n_{eff}^2}\right) = -\frac{n_2^2 - n_{eff}^2}{n_1^2 - n_{eff}^2}, \quad \text{for odd modes,}$$

where

$$n_{eff} = \frac{\beta}{k_0}. \tag{3.34}$$

The equations are transcendental, meaning that they have to be solved numerically using computer software or a calculator.

The equations can also be solved graphically by combining (3.13) and (3.17) into

$$k_x^2 + \alpha^2 = k_0^2(n_2^2 - n_1^2), \tag{3.35}$$

or if multiplied by d^2:

$$(k_x d)^2 + (\alpha d)^2 = (k_0 d)^2 (n_2^2 - n_1^2). \tag{3.36}$$

Equation (3.36) represents a circle with a radius

$$R = k_0 d \sqrt{n_2^2 - n_1^2}, \tag{3.37}$$

where d is half of the waveguide thickness, and n_2 and n_1 are the indices of refraction of the dielectric medium and the cladding, respectively. Values for α and k_x can be determined by plotting the circle together with the tangential and cotangential functions (multiplied by d) and finding the intersection points. These values can then be used to find β and n_{eff} for each wave mode.

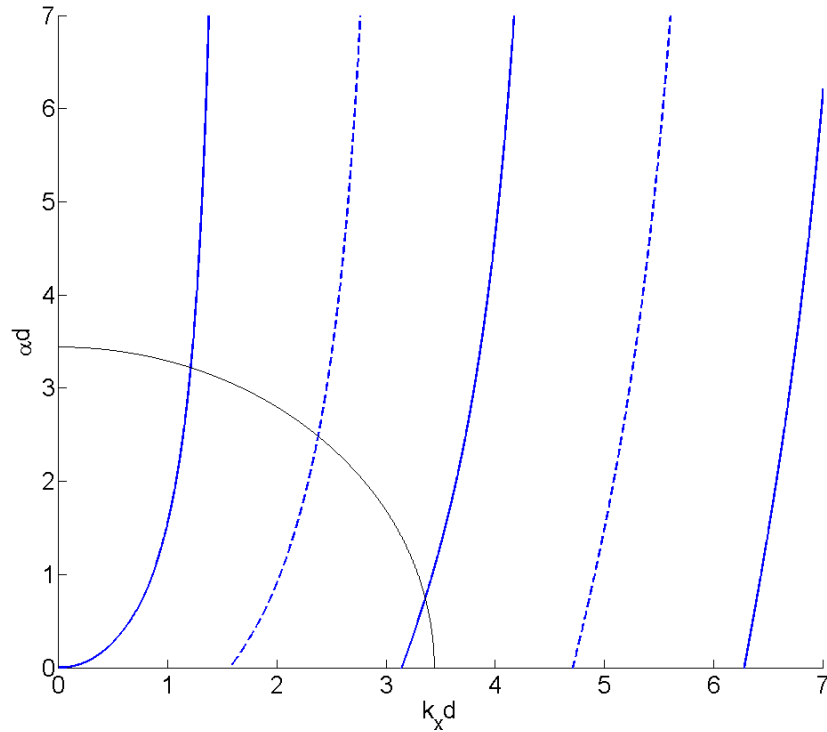The graphical solution is illustrated in Figure 3.

Figure 3: Illustration of the graphical solution of phase constant and effective index of refraction. The solid blue lines correspond to the even modes, dashed blue lines represent the odd modes, and the solid black line is a circle with a radius *R* defined by (3.37).

3.2.3. TM modes

The process for finding the fields of the TM modes is very similar to the case of the TE modes. Now the magnetic field is oriented into the *y*-direction and the electric field has *x*- and *z*-components. The equation for the magnetic field is

$$H_y(x, y) = H_m(x)e^{-j\beta y}, \tag{3.38}$$

where $H_m(x)$ is the solution to the wave equation

$$H_m(x) = \begin{cases} A\sin(k_x x) + B\cos(k_x x) & |x| < d \\ Ce^{-\alpha x} & x > d \\ De^{\alpha x} & x < -d, \end{cases} \tag{3.39}$$

where α and k_x are defined the same way as in the case of TE modes. Again, boundary conditions are applied and the conditions for symmetric and anti-symmetric TM modes become

$$
\begin{cases}
\alpha = \dfrac{n_2^2}{n_1^2} k_x \tan(k_x x) & \text{even modes} \\[2ex]
\alpha = -\dfrac{n_2^2}{n_1^2} k_x \cot(k_x x) & \text{odd modes.}
\end{cases}
\tag{3.40}
$$

It is worth noting that if the DSW is surrounded by air, i.e., $n_1 = 1$, the conditions for the TE and TM modes are the same.

3.3.   Cut-off frequency

Equation (3.37) can be used to determine the cut-off frequency for each wave mode if the waveguide thickness is known. Conversely, if the operating frequency is known, the minimum waveguide thickness for each mode can be determined. Radius R can be replaced with $m\pi/2$ (zeros of the tangential and cotangential functions), where m corresponds to the studied mode, TE_m or TM_m. In order to find the cut-off frequency f_c, (3.37) can be re-ordered into

$$
\frac{2\pi f_c}{c_0} = \frac{\dfrac{m\pi}{2}}{d\sqrt{n_2^2 - n_1^2}} \Rightarrow f_c = \frac{m c_0}{4 d \sqrt{n_2^2 - n_1^2}} ,
\tag{3.41}
$$

where $2d$ is the thickness of the lens, n_1 and n_2 are the indices of refraction of the surroundings and the dielectric medium, and c_0 is the speed of light in a vacuum. The equation shows that for the fundamental wave modes TM_0 and TE_0 the cut-off frequency is 0 Hz, meaning that they are always propagating and guided. This indicates that there are no theoretical limitations regarding the minimum thickness of the waveguide, which can be beneficial when designing 2-D lens structures.

It is often desired that only the fundamental wave mode is propagating so the higher order wave modes do not disturb the operation of the waveguide. Equation (3.41) can be used to find the maximum thickness for single-mode propagation if the operating frequency f is known:

$$
d_{max} = \frac{c_0}{4 f \sqrt{n_2^2 - n_1^2}} .
\tag{3.42}
$$

4. Lens design

For this study, teflon and a commercial plastic preperm450 were chosen as lens materials. Teflon is commonly used as a material for dielectric lenses due to its reasonably low price and low dielectric losses. Preperm450 is a low-loss plastic material developed for high frequency antenna applications by Premix corporation [34]. The dielectric properties of preperm450 were measured at $50-110$ GHz in [35] and were found to be

$$\varepsilon_r = 4.48 \text{ and } \tan \delta = 0.009.$$

For Teflon the corresponding values are [36]

$$\varepsilon_r = 2.06 \text{ and } \tan \delta = 0.00022.$$

The lenses were designed for TM polarization and the mode of operation is the fundamental mode TM_0. The lenses are placed in the *xy*-plane and the direction of propagation is the *y*-direction. For TM-polarization this means that the electric field is polarized into the direction of *z*-axis, and E- and H-planes lie in *yz*- and *xy*-planes, respectively. The Cartesian and spherical coordinate systems are defined in Figure 4.
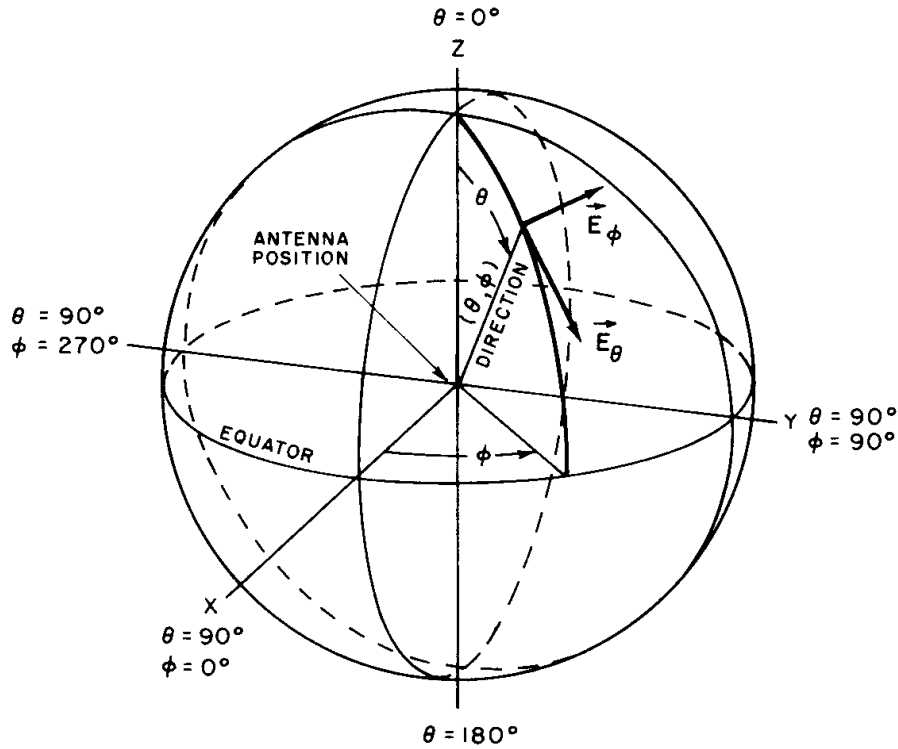
Figure 4: Cartesian and spherical coordinate systems [37].

The lens is fed with a rectangular WR-10 waveguide, which has dimensions of 1.27 mm * 2.54 mm and operates at W-band (75 − 110 GHz). Waveguide feed was chosen due to its simplicity and easy implementation in the measurements.

In order to achieve a more realistic measurement environment, the antenna should not be assumed to be surrounded by air. Due to the surface waves the surrounding material should be as lossless as possible in order to avoid significant gain reductions. On the other hand, according to the equations derived in Section 3.1 the index of refraction of the surrounding medium (n_1 in Figure 2) affects the propagation characteristics of the lens, so low relative permittivity is desired as well.

Rohacell® HF, developed by Evonik Industries, is a family of rigid and lightweight structural foam materials designed for RF applications, especially for antennas [38]. The dielectric properties of the used material were measured at W-band in [39] and found to be

$$\varepsilon_r = 1.069 \text{ and } \tan\delta = 0.0028.$$

The lens is eventually placed between two 5 mm sheets of Rohacell® HF.

The most important consideration in the lens design is the shape of the lens. It should be chosen as such, that the spherical wave, radiated by the feed antenna, is converted into a plane wave. In this study this behavior is implemented by shaping the lens as an extended hemi-ellipse. The same lens configuration has been applied before in, e.g., [2] and [26]. The illustration of the lens structure and formation of the plane wave is presented in Figure 5, and the design equations are presented in the following.

General equation for an ellipse in the *xy*-plane is

$$\left(\frac{x}{a}\right)^2 + \left(\frac{y}{b}\right)^2 = 1, \tag{4.1}$$

where *a* and *b* are the minor and major axes, respectively. The focus points lie at

$$c = \pm\sqrt{b^2 - a^2}, \tag{4.2}$$

which also gives, in theory, the optimal length of the dielectric extension *L*. [25]
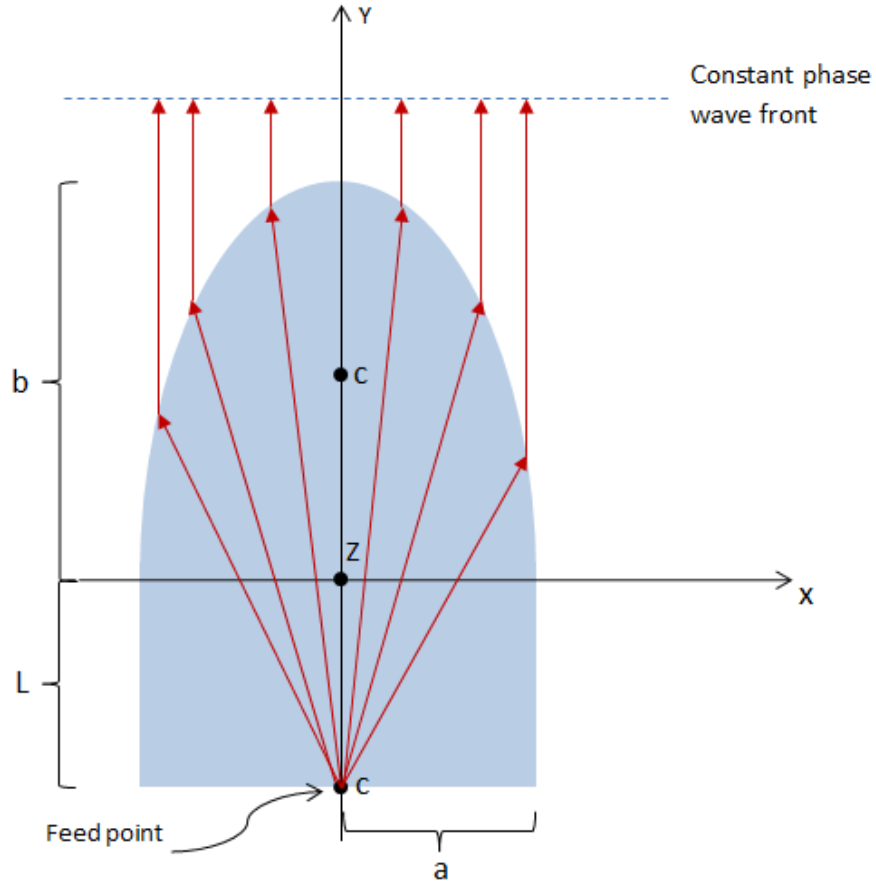
Figure 5: Lens structure and the formation of the plane wave [14].

From optics it is known that the eccentricity, i.e., the measure of circularity, *e* of an ellipse is defined as

$$e = \frac{c}{b} = \frac{\sqrt{b^2 - a^2}}{b} = \frac{1}{n_{eff}}, \qquad (4.3)$$

where n_{eff} is the effective index of refraction of the lens material [26, 33]. Now the relation between *a*, *b*, and *c* can be derived as

$$a = b\sqrt{1 - \frac{1}{n_{eff}^2}} \quad \text{and} \quad c = L = \frac{b}{n_{eff}}. \qquad (4.4)$$

In reality, the value for the dielectric extension suggested by (4.4) is not optimal because the phase center of the waveguide feed is not located at the end of the waveguide, like is assumed in the above

analysis. This means that *L* needs to be tuned in order to optimize the operation of the antenna. The optimal value for *L* can be found with computer simulations.

The maximum thickness for single-mode propagation at E-band (f_{max} = 86 GHz) can be calculated from (3.42):

$$2d_{max} = \begin{cases} 0.94 \text{ mm} & \text{for preperm450} \\ 1.75 \text{ mm} & \text{for teflon.} \end{cases}$$

In order to ensure the single-mode propagation over the whole band, the lens thicknesses were chosen to be 1.00 mm for teflon lens and 0.80 mm for preperm450 lens. This results in the cut-off frequency for the first higher-order wave modes to be above 100 GHz in both cases. Furthermore, the thickness of each lens is electrically small enough (approximately $\frac{1}{4}\lambda_0$ at 78.50 GHz) for the lenses to be treated as 2-D structures. Minor axis was chosen to be *a* = 25 mm. Figure 6 shows the effective index of refraction for TM_0 mode as a function of frequency at 70 – 90 GHz.
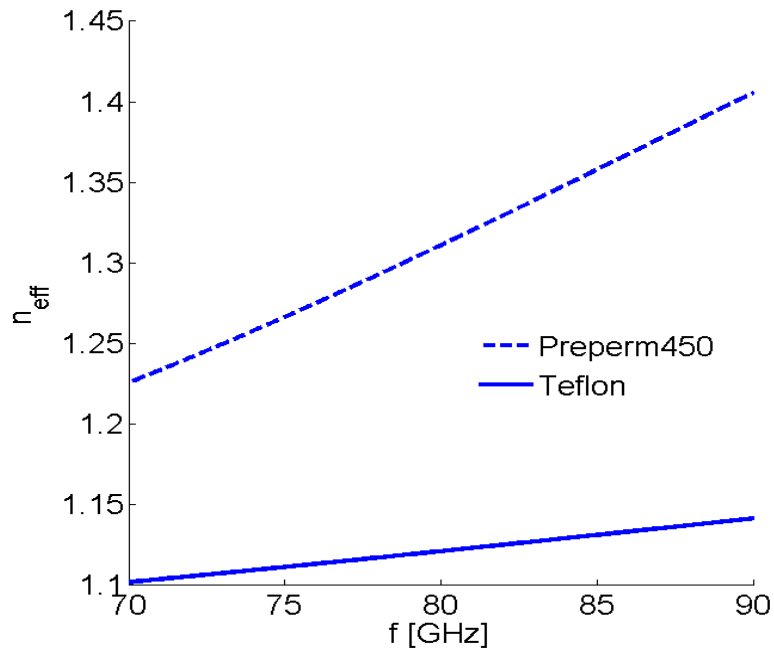

Figure 6: Effective index of refraction as a function of frequency.

Because n_{eff} is frequency-dependent, physical dimensions of the lens depend on the frequency as well. This indicates that a lens designed for one frequency is not guaranteed to operate correctly at another frequency. This needs to be considered in the design process when the lens antenna is

desired to operate over a frequency band rather than at a single frequency. In order to minimize the frequency offset, the center of the E-band was chosen as a design frequency. From Figure 6 it can be estimated that at 78.5 GHz

$$n_{eff} = \begin{cases} 1.30 & \text{preperm450} \\ 1.12 & \text{teflon} \end{cases},$$

which can then be used to calculate the physical dimensions of the lens using (4.4). The results are presented in Table 1.

Table 1: Physical dimensions of the designed lenses.

Material	Thickness [mm]	a [mm]	b [mm]	$c = L$ [mm]
Teflon	1.00	25	55.9	50.0
Preperm450	0.80	25	39.3	30.3

It was discussed earlier that the cut-off frequency for the fundamental wave modes is 0 Hz, which means that theoretically the wave can propagate in any DSW regardless of the thickness. However, other limitations regarding the minimum thickness of the lens exist. From Figure 6 it can be seen that the effective index of refraction is smaller at lower frequencies, eventually reaching 1.0 when the thickness of the DSW, or the lens, reaches 0. According to (4.4), decrease of n_{eff} causes the size of the lens to increase, which is undesirable when considering antenna solutions for portable applications. Reduced antenna aperture also widens the beam, hence lowers the directivity and gain. Furthermore, according to Snell's law, the angle of refraction depends on the indices of refraction, and higher n yields larger angle of refraction. This becomes an essential consideration in the design of beam steering applications. Higher index of refraction could also be achieved by using materials with higher permittivities, such as silicon or quartz, but this often results in higher losses and lower gain. A compromise should be found between the beam steering properties and physical dimensions of the lens while ensuring a high gain and single mode propagation at the desired frequency band.

5. Electromagnetic simulations

HFSS (High Frequency Structure Simulator), developed by Ansys Inc. [40] is used to conduct the electromagnetic (EM) simulations. HFSS is one of the leading EM simulators in the industry and it is often used in antenna simulations similar to the ones performed in this study. Operation of HFSS is based on finite element analysis (FEA), an application of finite element method (FEM), which is a numerical technique for solving complex differential and integral equations. In FEA the studied structure is divided into small sub-structures (meshing) which can be solved individually and then combined to find the approximate solution for the whole structure. [41]

Simulation model of the lens antenna constructed in HFSS is presented in Figure 7. Figure also shows the mesh generated by HFSS.
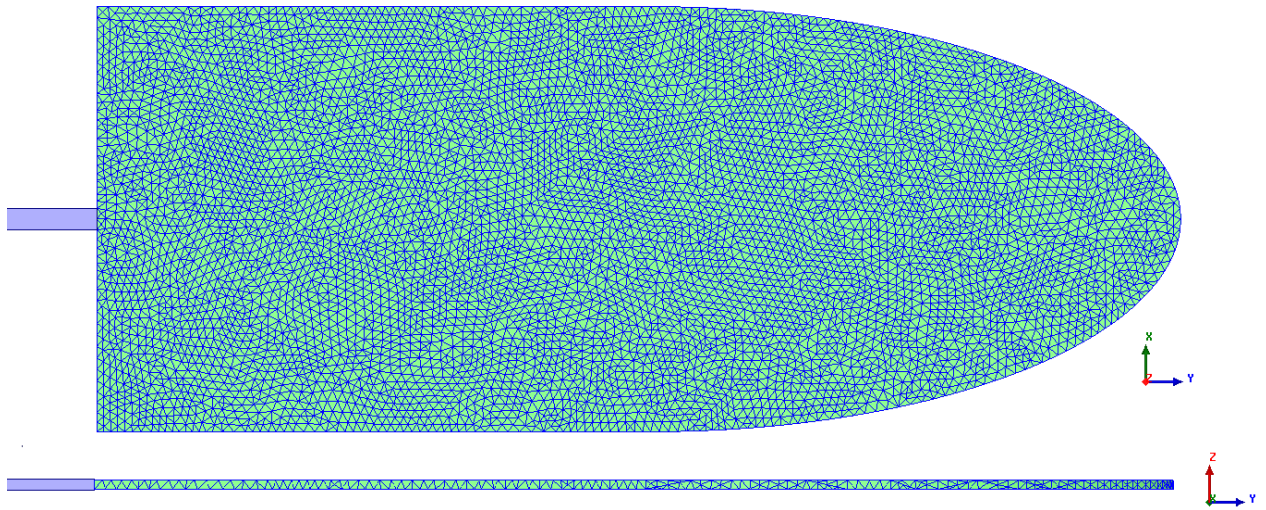
Figure 7: Simulation model of the dielectric lens antenna built in HFSS.

5.1.   Optimization of the dielectric extension

As mentioned before, an open-ended waveguide is not an isotropic radiator, thus the extension length *L* needs to be tuned in order to maximize the gain and the shape of the far-field pattern. This is done by replacing *L* with *L + ΔL*, where *ΔL* is the difference between the value suggested by theory and the optimal value. HFSS optimization tool can be used to find the value for *ΔL* which maximizes the gain. H-plane patterns for Teflon and preperm450 lenses with different values of *ΔL* are shown in Figure 8 and Figure 9.
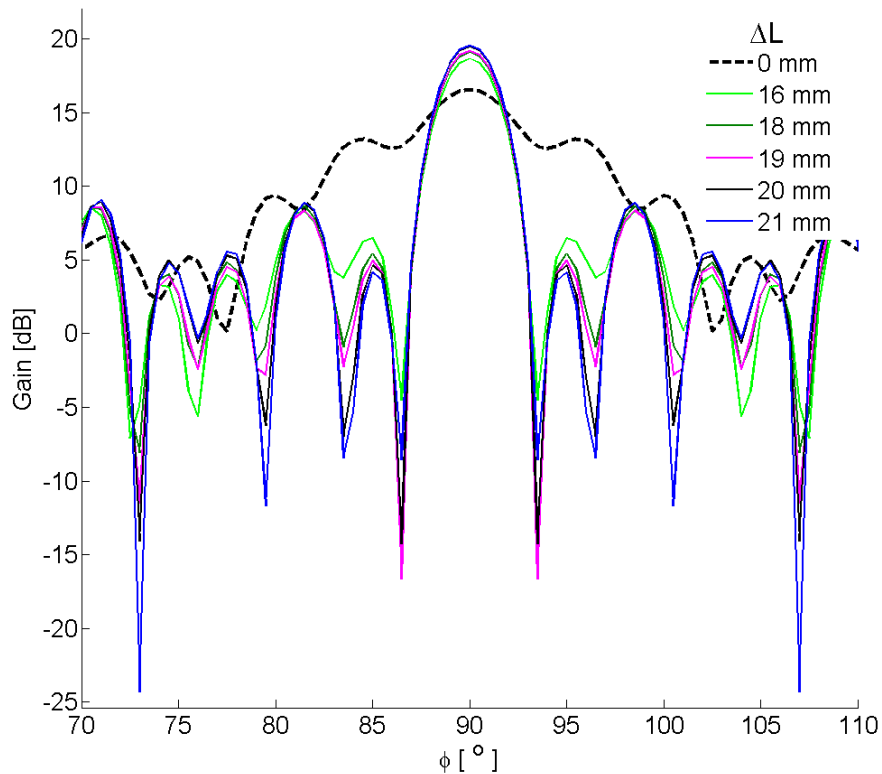
Figure 8: Effect of varying extension length on H-plane gain pattern of teflon lens at 78.5 GHz.
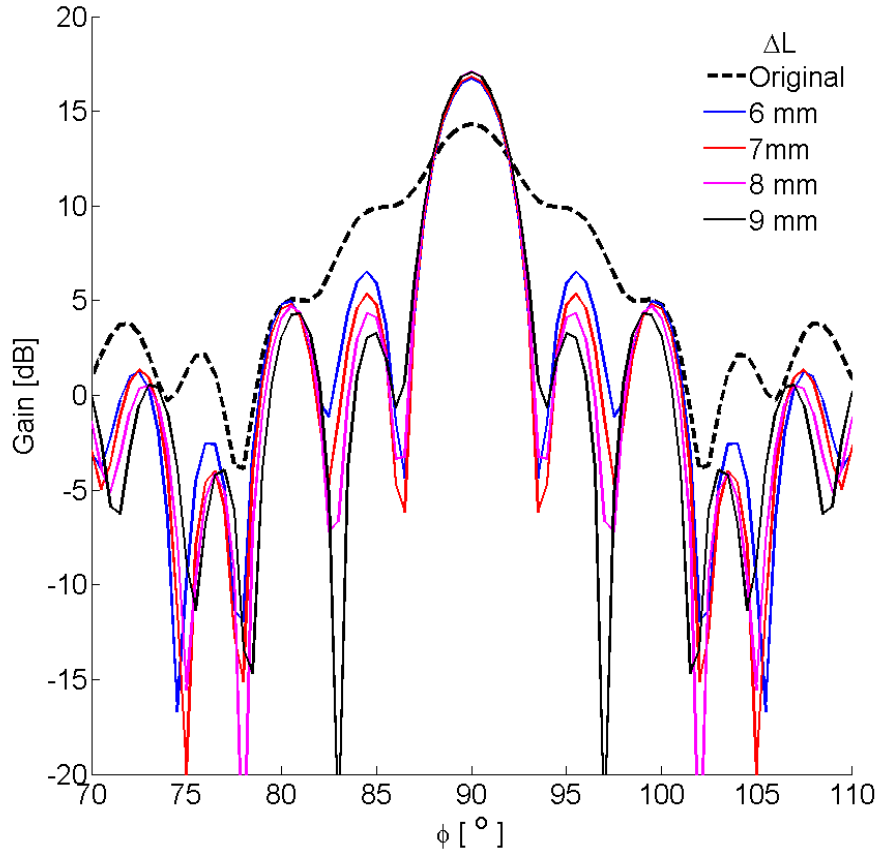
Figure 9: Effect of varying extension length on H-plane gain pattern of preperm450 lens at 78.5 GHz.

Figures show that the maximum gain is achieved when ΔL is 20 mm for teflon lens and 8 mm for preperm450 lens. Respective gains are 19.5 dB and 17.1 dB while the first side lobe levels (FSLL) are -14.9 dB and -12.9 dB compared with the main beam. The half-power beam-widths (HPBW, or ϕ_{3dB} and θ_{3dB}) are 3.4° and 3.3° in H-plane and 22.2° and 24.3° in E-plane, for teflon and preperm450 lenses, respectively.

Figure 10 shows the reflection coefficients of both lenses at E-band. As can be seen from the figure, the matching between the waveguide feed and the lenses is relatively poor at E-band. The matching is still good enough for the far-field results to be reliable and hence the improving of the matching is outside the scope of this thesis. It is worth noting that in real-life applications where the waveguide feed is replaced with, e.g., a microstrip patch antenna array, the matching should be improved significantly.
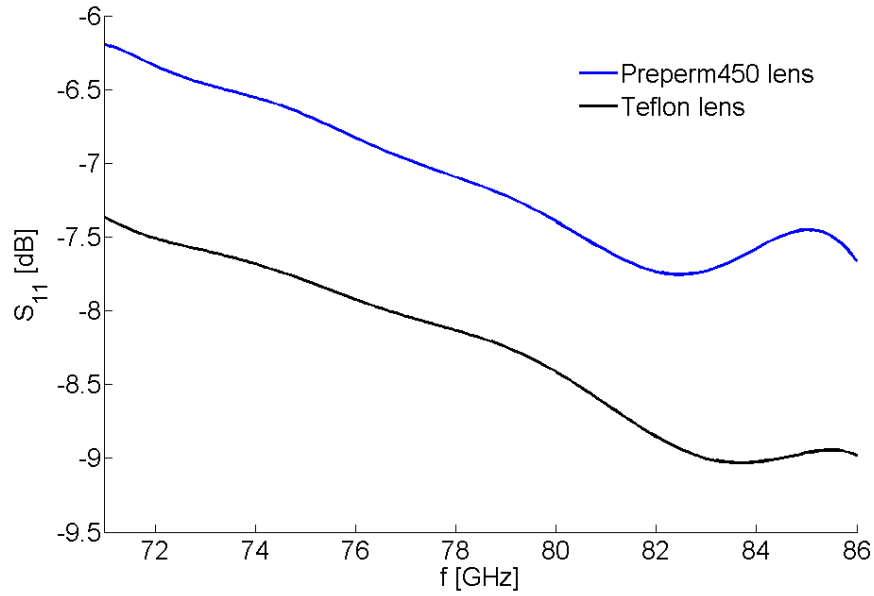
Figure 10: Reflection coefficient S_{11} of both lenses at E-band.

5.2.   Microwave absorbers

In order to finalize the design, microwave absorbers should be included in the simulation model. Absorbers are very lossy materials with typical reflectivity of < -50 dB at mm-wave frequencies. They are used to attenuate the radiated field outside the main lobe and to isolate the device under test (DUT) from the surroundings. Absorbers are also used to capture the power radiated from the extension part (spill-over field) ensuring that only the field radiated by the collimating part of the lens affects the far-field pattern. [42]

Figure 11 shows the positioning of the absorbers around the antenna and Figure 12 and Figure 13 show the effect of the absorbers on the far-field patterns.
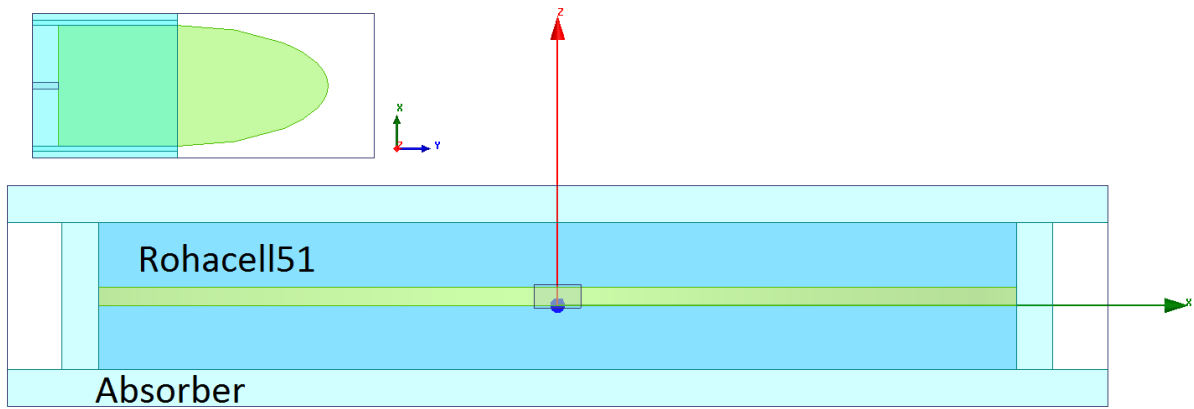
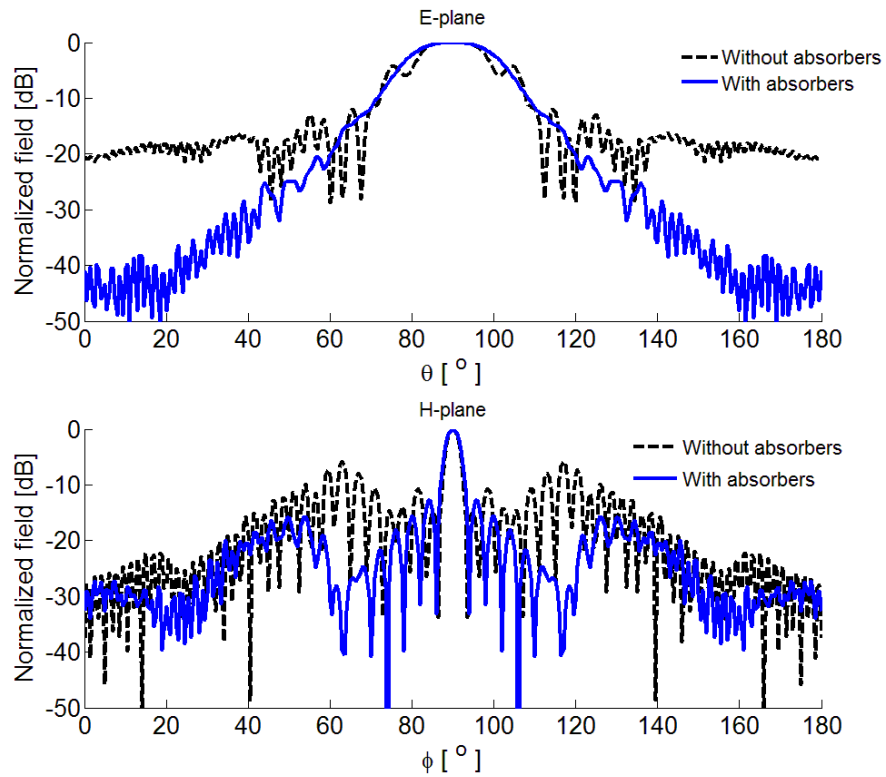Figure 11: Positioning of the Rohacell supporting foam and microwave absorbers.

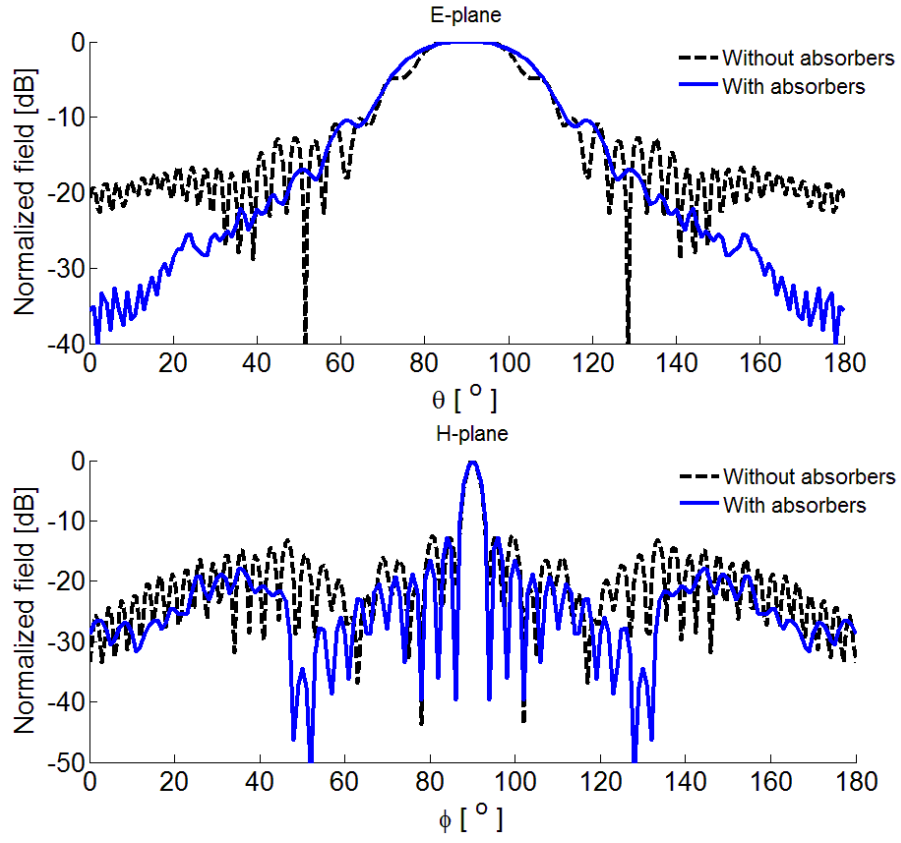Figure 12: Effect of microwave absorbers on radiation pattern of the teflon lens at 78.5 GHz.

Figure 13: Effect of microwave absorbers on radiation pattern of the preperm450 lens at 78.5 GHz.

6. Other lens configurations

In addition to the antenna designed and studied in Chapter 4 and Chapter 5, some other lens structures are studied as well. First structure, parallel plate lens, is similar to the original lens structure but it is shielded from the top and bottom with metal plates, removing the effect of the surrounding material. With parallel plates permittivity corrections are not required which decreases the size of the lens. The theory behind parallel plate lenses and the design process is presented in Section 6.1. Section 6.2 concentrates on a thicker version of the preperm450 lens with possibly multiple propagating wave modes. While ensuring single-mode propagation would be ideal, practical limitation prevent the manufacturing of a single-mode preperm450 lens. A thick parallel plate lens antenna is designed as well. A comparison between the two lens configurations is performed in Section 6.3

6.1.   Parallel plate teflon lens

The structure of a parallel plate lens antenna is similar to the one presented before but in this case the extended hemi-ellipse is shielded between two parallel metal plates. Due to the orientation of the electric field for TM polarization, permittivity does not need to be corrected and index of refraction of the material

$$n_{eff} = n = \sqrt{\varepsilon_r} \tag{6.1}$$

is used in the lens design. [21]

Higher index of refraction presents several benefits. Firstly, according to (4.4), the physical dimensions of the lens become smaller. Secondly, the frequency-dependence of the index of refraction almost disappears (only the inherent dependency is left) allowing for more broadband solutions. Lastly, metallic walls guarantee that there is no interaction between the fields and the surroundings.

Operation of the parallel plate lens antenna is based on a parallel plate waveguide (PPW) filled with dielectric material (Figure 14).
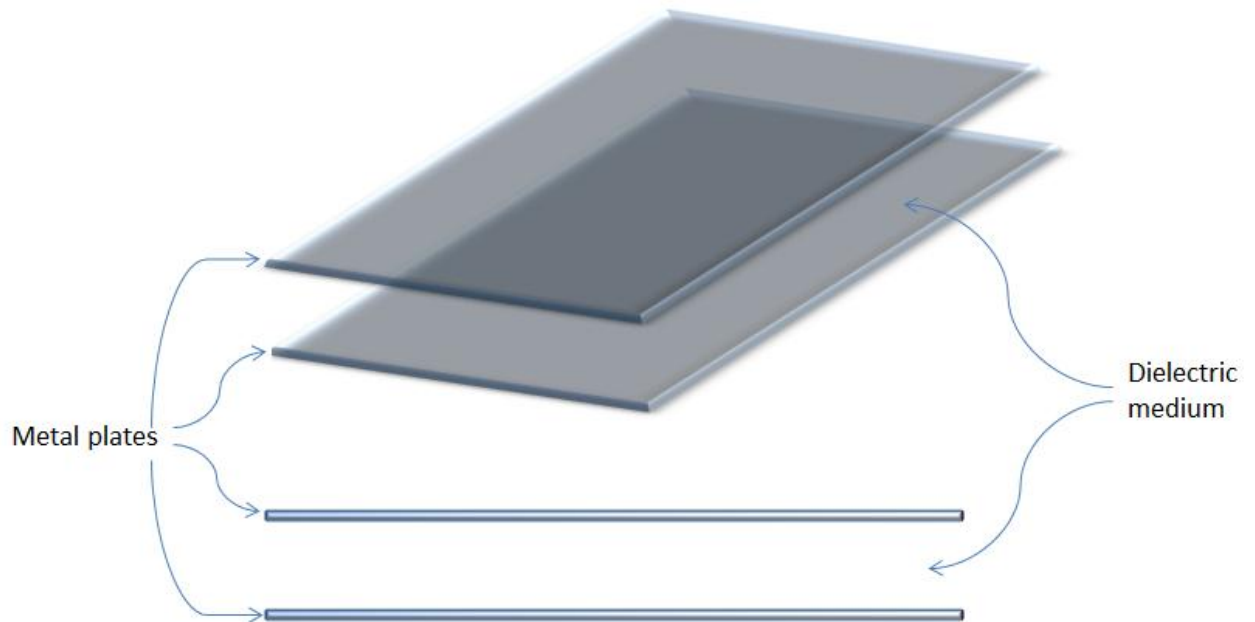

Figure 14: Schematic of a parallel plate waveguide.

The analysis of a parallel plate waveguide is similar to that of a traditional rectangular waveguide (Figure 15) and detailed field analysis can be found from the literature, e.g., [43, 44] ,. However, the condition for the cut-off frequencies change, and can be derived from that of a rectangular waveguide [31]

$$f_{c,mn} = \frac{c}{2\pi}\sqrt{\left(\frac{m\pi}{a}\right)^2 + \left(\frac{n\pi}{b}\right)^2},$$

(6.2)

Where c is the speed of light, a and b are the waveguide dimensions, and m and n refer to the wave mode in question.
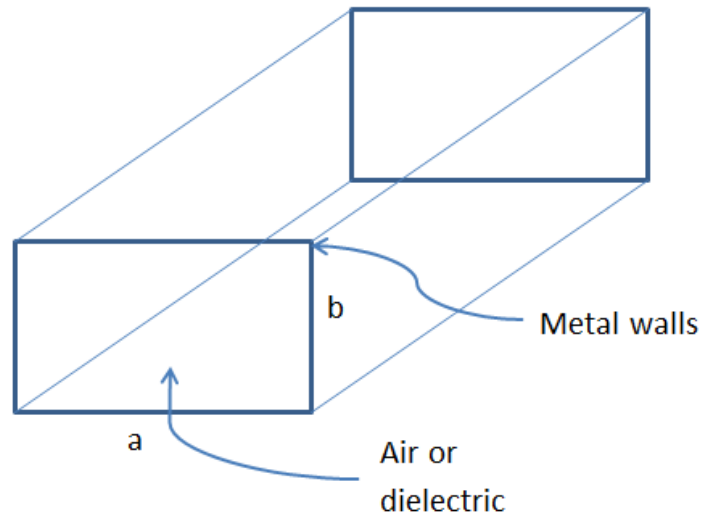
Figure 15: Rectangular waveguide.

If a is large compared to b, like in the case of a PPW, the cut-off frequency can be written as

$$f_{c,n} = \frac{c}{2\pi}\left(\frac{n\pi}{b}\right),$$ (6.3)

where n is the order of the wave mode and b is the thickness of the waveguide. For the fundamental modes the cut-off frequency is again at 0 Hz, while for higher-order wave modes it depends on the thickness of the waveguide and the relative permittivity of the dielectric medium:

$$f_{c,n} = \frac{nc_0}{2b\sqrt{\varepsilon_r}}.$$ (6.4)

6.1.1. Lens design and simulation

The geometry of a parallel plate lens is essentially the same as without metallic shielding, meaning that the same equations can be used in design of physical dimensions of the lens. Width of the lens is kept unchanged at 50 mm. For teflon n = 1.435, which yields, using (4.4),

$$b = 34.9 \text{ mm} \quad \text{and} \quad c = L = 24.3 \text{ mm.}$$

Thickness of the lens is kept at 1.00 mm setting the cut-off frequency of the first higher order wave mode at 104 GHz. In the simulation model 1.0 mm thick copper plates are used to model the parallel plates. Figure 16 shows the simulation model of the parallel plate lens built in HFSS. Figure 17 shows

the E- and H-plane gain patterns of the designed parallel plate teflon lens. Gain of the antenna is 18.1 dB, H-plane FSLL is -12.7 dB, and HPBW in E- and H-plane are 35.5^o and 3.9^o, respectively.
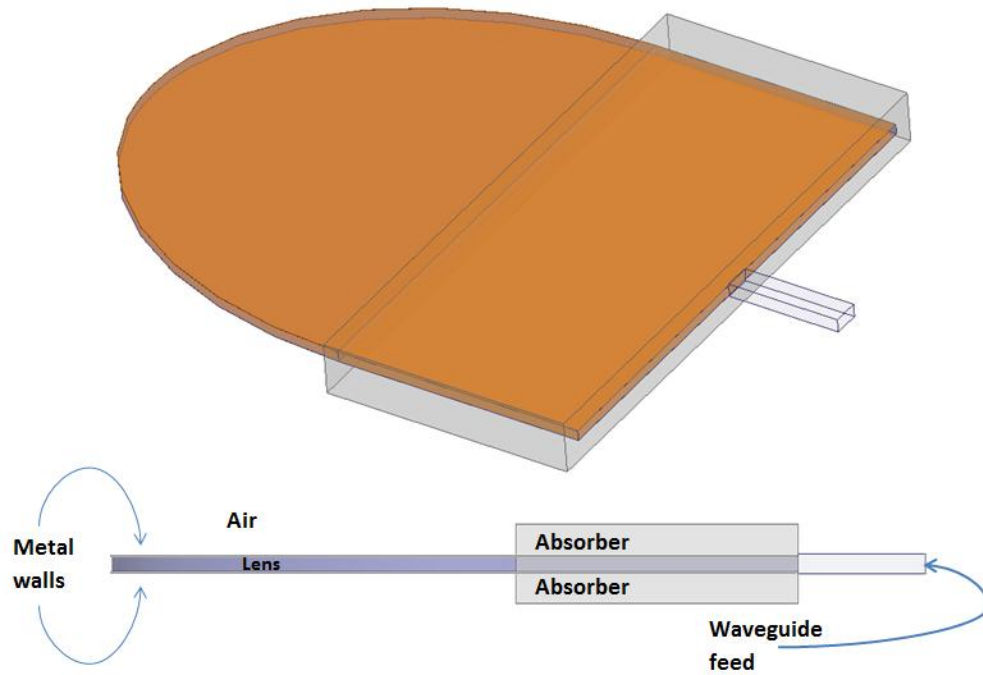

Figure 16: HFSS simulation model of the parallel parallel plate lens antenna.
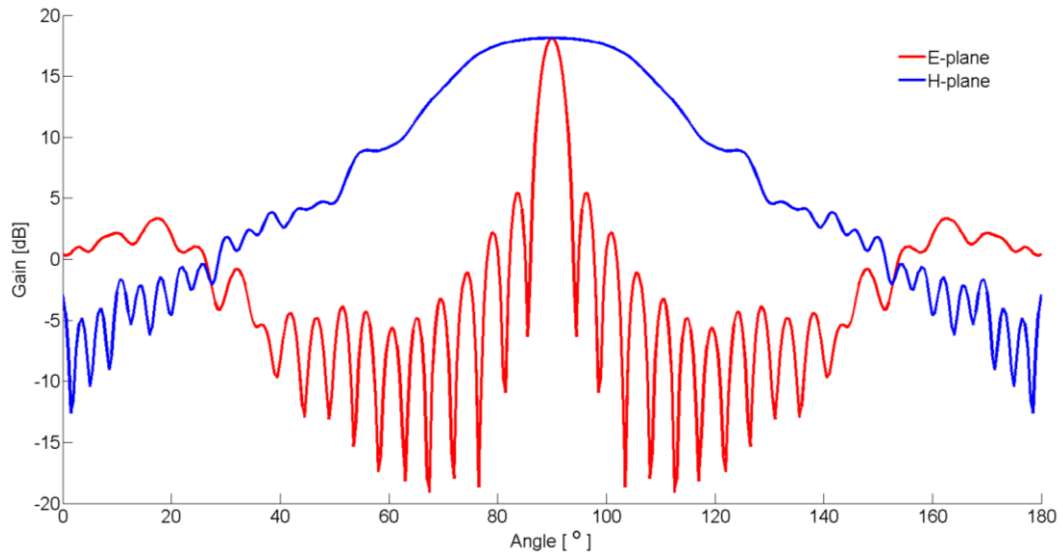

Figure 17: E- and H-plane radiation patterns of the parallel plate teflon lens at 78.5 GHz.

6.2. Thick preperm450 lens

Even though single-mode propagation is usually desired, it is not always feasible or practical to realize an antenna with that characteristic. The thickness of the preperm450 material sample was 3.00 mm and it is examined how the possible higher order wave modes affect the radiation pattern if the lens is made 3.00 mm thick. Using (3.33) shows that n_{eff} = 2.046 at 78.50 GHz which yields lens dimensions of b = 28.7 mm and $c = L$ = 14.0 mm, and three possible propagating TM modes (Figure 18).
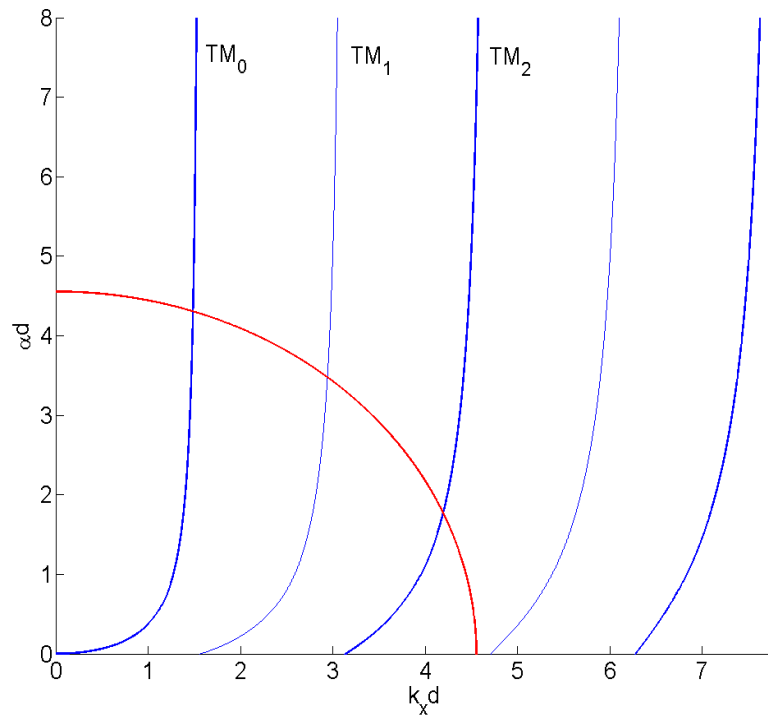

Figure 18: Graphical solution of the TM wave modes in the thick preperm450 lens.

Figure 19 shows the radiation patterns in both E- and H-plane. The corresponding patterns of the 0.8 mm thick preperm450 lens are plotted in the same figure for comparison and to confirm the absence of the higher order wave modes.
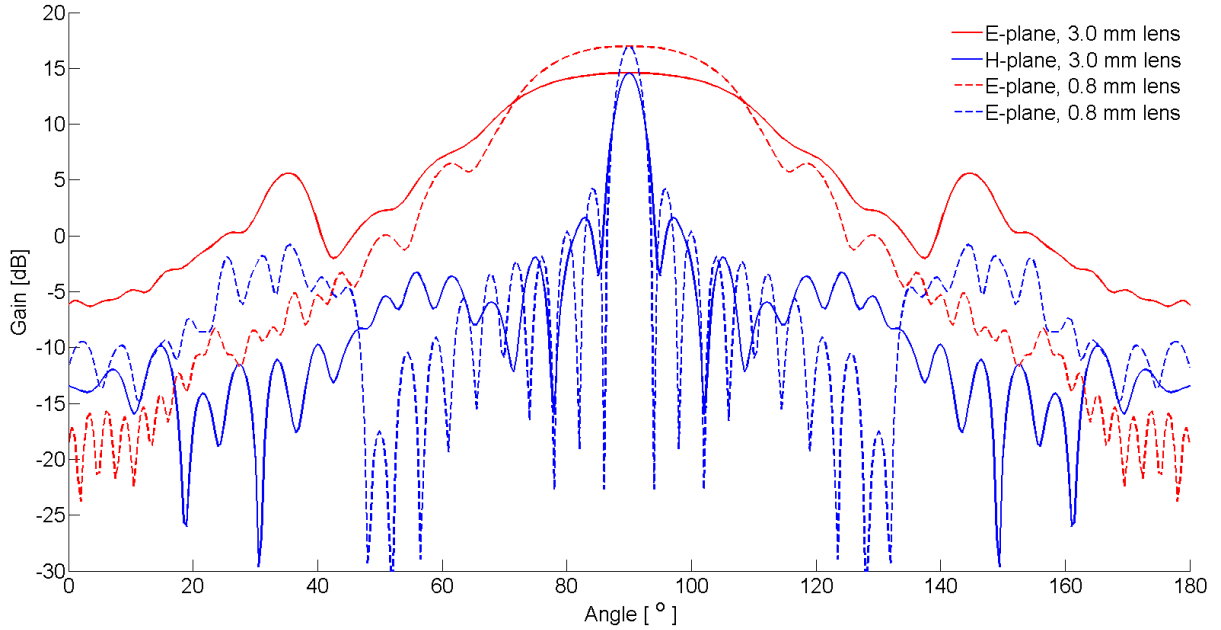
Figure 19: E- and H-plane radiation patterns of the 0.8 mm thick and 3.0 mm thick preperm450 lenses at 78.5 GHz.

The maximum gain is achieved with ΔL = 1 mm and is 14.6 dB. The HPBWs are 4.2^o and 38.6^o in H- and E-plane, respectively, and H-plane FSLL is -13.0 dB. The biggest differences between the two lenses are in the bandwidth and gain. These differences are not analyzed further because, based on the gain and the shape of the far-field pattern of the 3.0 mm lens, the higher order wave modes do not seem to be excited, or at least are not interfering with the operation of the antenna.

6.2.1. Thick preperm450 lens with parallel plates

Parallel plate version of the thicker preperm450 lens is designed as well. Design equations yield dimensions of b = 28.4 mm, c = L = 13.4 mm, while a = 25 mm. Again, the parallel plates are realized with 1.0 mm thick copper plates. Figure 20 shows the gain patterns in the H- and E-plane. Antenna gain is 12.5 dB, H-plane is FSLL -19.4 dB, and HPBWs are 4.5^o and 28.8^o in H- and E-plane, respectively.
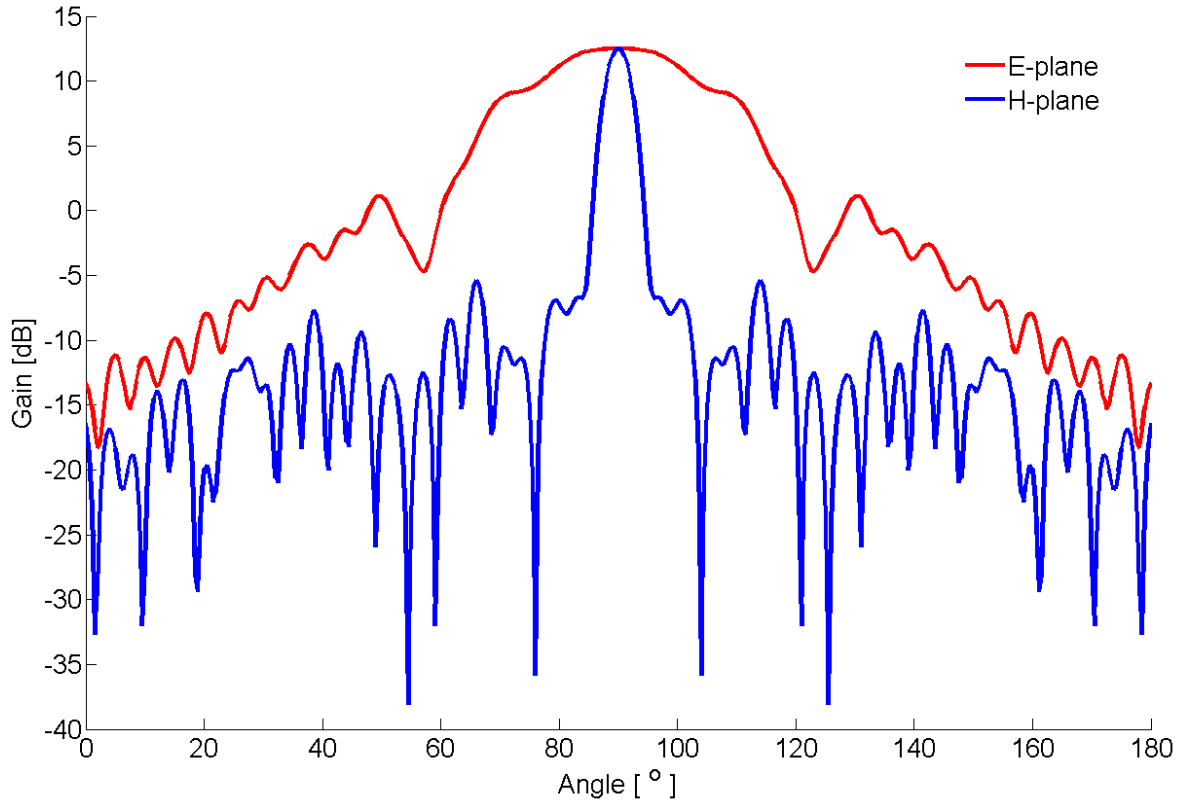
Figure 20: E- and H-plane radiation patterns of the thick preperm450 lens with parallel plates at 78.5 GHz.

6.3.   Comparison between the two lens configurations

Comparison of the radiation patterns of the two studied lens configurations show significant differences in beamwidth and gain. Like discussed in Chapter 3, in a dielectric slab waveguide the waves travel mostly as surface waves. However, in a parallel plate waveguide this is not possible because the metal plates enclose the waves completely into the dielectric. This has two main outcomes. Firstly, the effective aperture of the antenna in z-direction is reduced, which, in theory, results in a larger beamwidth in E-plane. Wider beam means lower directivity D, which translates into a lower gain. Secondly, while in a DSW only dielectric losses are present, in a PPW some conductive losses are introduced by the non-zero skin depth of the metal walls. The overall losses can be evaluated by studying the differences between the amplitudes of directivity and gain. Directivity and

gain patterns of all studied antennas at 78.5 GHz are presented in Figure 21 and Figure 22. Losses are calculated from the figures and listed in Table 2.
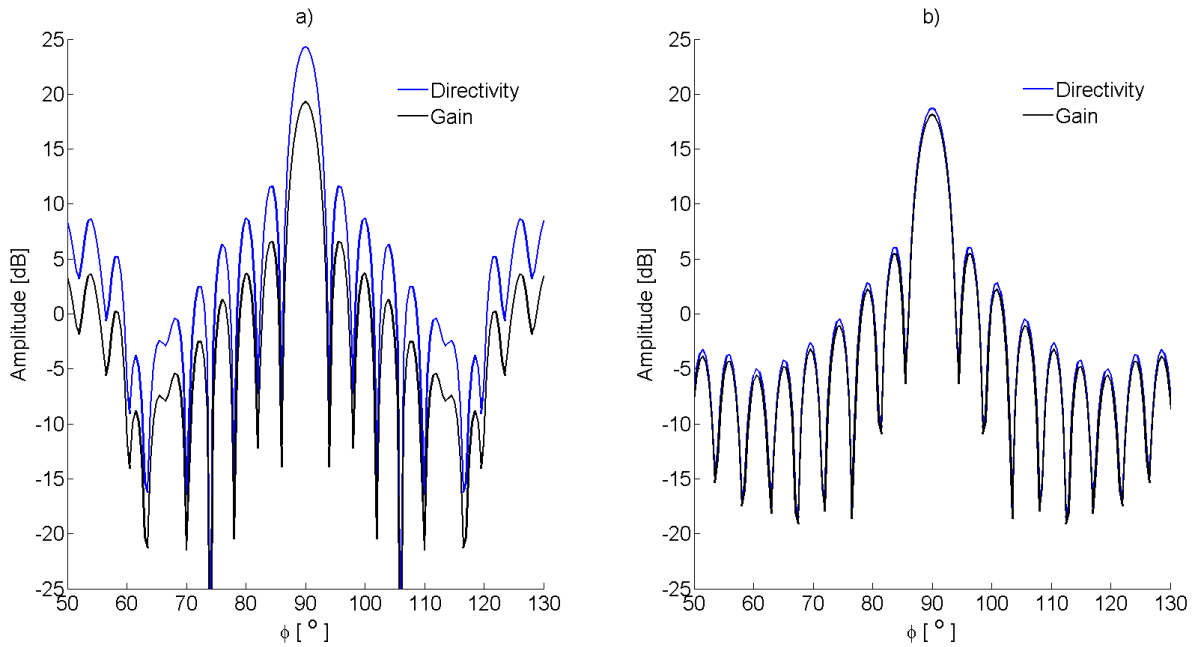

Figure 21: Directivity and gain of the teflon lenses. a) DSW extended lens and b) parallel plate lens.
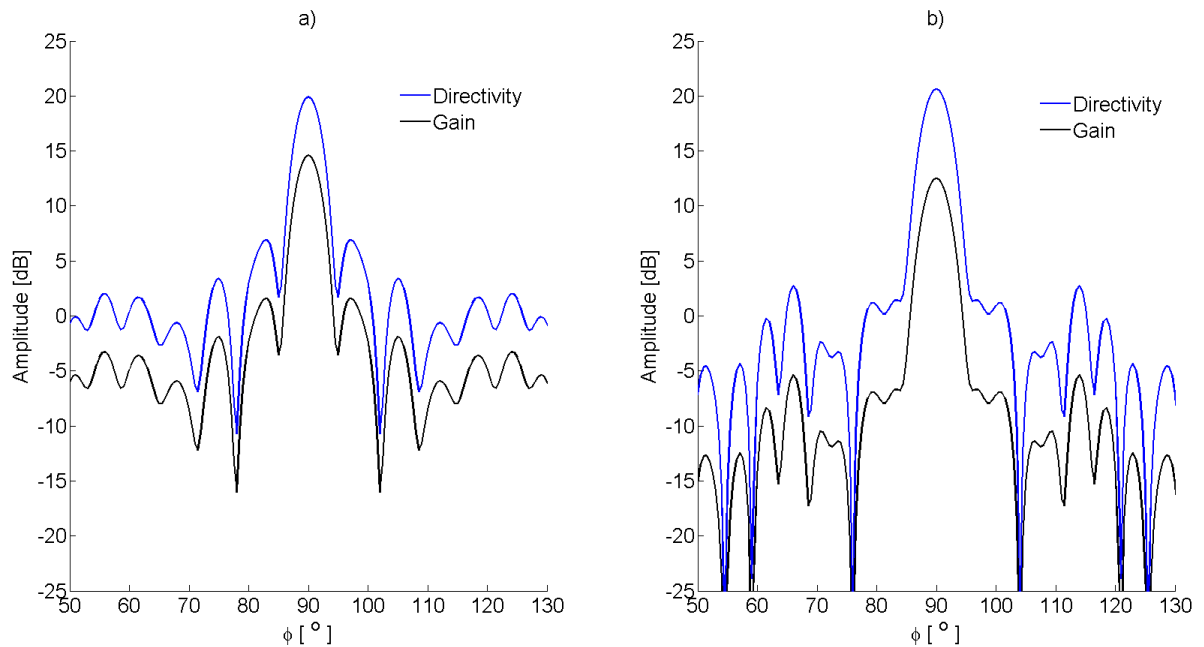

Figure 22: Directivity and gain of the preperm450 lenses. a) DSW extended lens and b) parallel plate lens.

Table 2: Losses and related parameters of the studied antennas.

Lens	D [dB]	G [dB]	Loss [dB]	S_{11} [dB]
DSW extended teflon	24.3	19.3	5.0	-8.2
Parallel plate teflon	18.7	18.1	0.6	-14.6
DSW extended preperm450	19.9	14.6	5.3	-4.9
Parallel plate preperm450	20.6	12.5	8.1	-5.4

The most interesting result is the loss of the parallel plate teflon lens which is significantly lower than the loss of any other lens. A correlation can be noticed between this and the matching, which is clearly the best in the case of the parallel plate teflon lens. Another main factor affecting the losses is the dielectric properties of the lens material. In general for teflon, the parallel plate version experiences significantly lower losses than the DSW extended lens, while the preperm450 lenses behave the exact opposite. This indicates that the dielectric loss tangent of teflon is so low that when the metallic walls enclose the waves completely into teflon, the dielectric losses are lower than when traveling partly as surface waves in Rohacell. The dielectric loss tangent of preperm450, however, is significantly larger, which means that in the parallel plate version the dielectric losses are also larger. These results indicate that the conductive losses caused by the metal plates are relatively small and dielectric losses dominate. This is also confirmed with simulations where the dielectric loss tangent of preperm450 is varied from 0.005 to 0.010. Figure 23 and Figure 24 show that the directivity remains close to unchanged while the difference in gain is more than 3 dB.
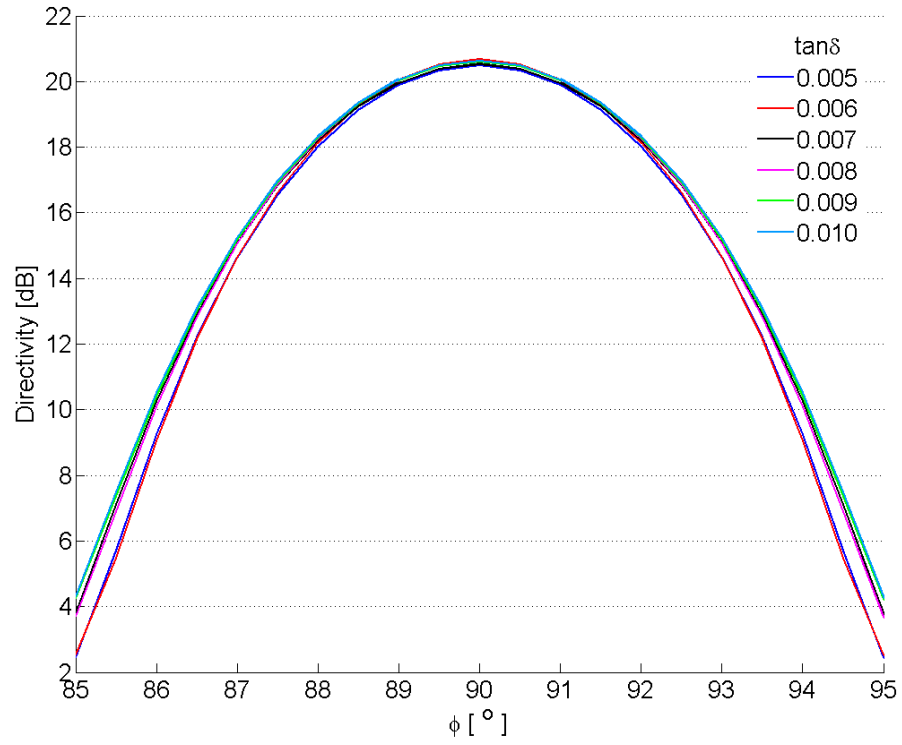
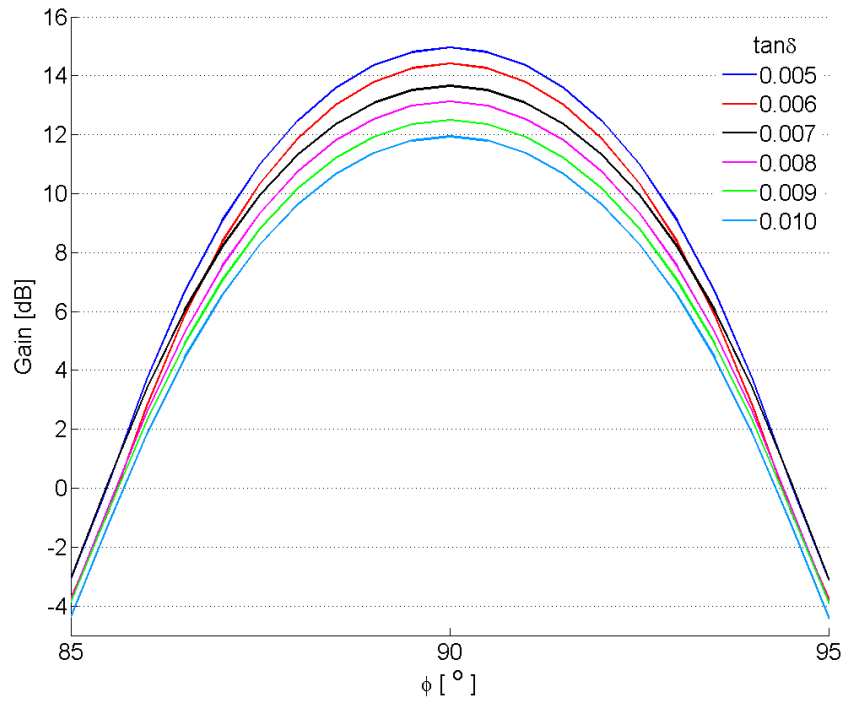Figure 23: Directivity of the parallel plate preperm450 lens with varying tanδ.

Figure 24: Gain of the parallel plate preperm450 lens with varying tanδ.

7. Measurements

This chapter focuses on the measurements. Section 7.1 provides a short introduction into the antenna far-field measurements in general. Some of the most common measurement techniques are described, including measurement technique used in this study, which is a near-field measurement using a planar near-field scanner. In Section 7.2 the manufactured antenna prototypes are presented and details of the measurement setup implemented for this work are provided.

7.1. Antenna measurements

The domain into which the antenna radiates can be divided into three separate regions depending on how the radiated field behaves (Figure 25). The regions are reactive near-field region, radiative near-field region (Fresnel region), and the far-field region (Fraunhofer region). In the reactive near-field region no distinctive radiation pattern exists and the non-radiating field components dominate. In the radiative near-field region a radiation pattern exists but is largely dependent on the distance between the source and the point of observation. In the far-field region the field distribution becomes independent of the distance and only depends on the direction of observation, meaning that the radiated field can be locally approximated as a plane wave and the field distribution is effectively the same as at $r \rightarrow \infty$ [45].
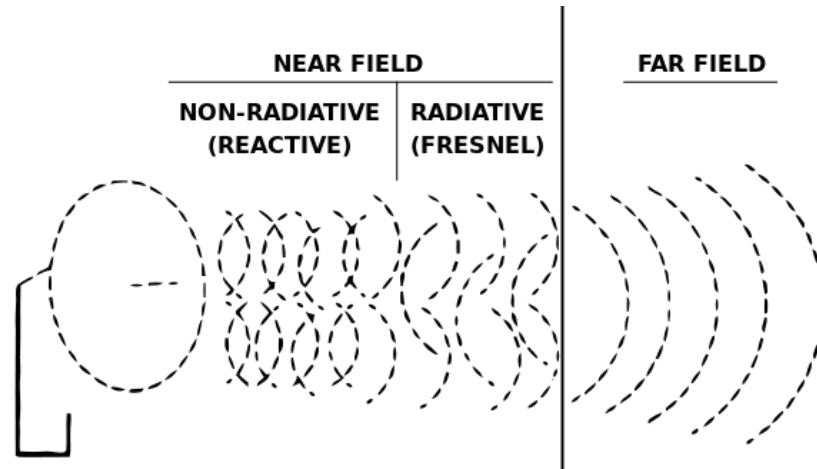
Figure 25: Illustration of the antenna field zones. [46]

In order to directly measure the far-field pattern of an antenna, the receiving antenna should be placed in the far-field region of the transmitting antenna under test (AUT). Usually the beginning of the far-field region is defined to begin at the so-called Fraunhofer distance [47]

$$r = \frac{2D^2}{\lambda},$$

(7.1)

where *D* is the largest antenna dimension.

At higher frequencies, as the wavelength shortens, the Fraunhofer distance can easily become so large that a direct measurement of the antenna far-field is not feasible except for the smallest antennas. The far-field distance becomes an issue for extremely large antennas as well, such as reflector antennas used in the field of radio astronomy. Moreover, even if the measurement setup could be implemented, the free-space losses may become too large as the distance between the receiver and AUT increases. [48]

Typically in these cases either a compact antenna test range (CATR) or near-field measurements are used to define the far-field of an antenna. In a CATR measurement a plane wave is formed by placing a collimating element, e.g., a reflector, a hologram, or a lens, between the AUT and the receiver. This way the far-field condition can be fulfilled in a laboratory environment. The main disadvantage of CATRs is the requirement for high surface accuracy of the collimating element, which makes the manufacturing difficult and expensive. [49, 50]

In this study the measurements are performed using a planar near field scanner to measure the near-field of the AUT, which can be used to calculate the far-field pattern of the antenna. Near field measurements are performed by placing a receiving antenna into the radiating near field region of the AUT. The receiver is used to collect the near field data by scanning a pre-defined area in front of the AUT. Based on the measurement data, the plane wave spectrum of the field can be calculated which represents the far-field pattern of the AUT. In order to increase the accuracy of the results, a probe correction is also performed on the measured pattern. This way the non-isotropic nature of the feed probe is taken into account. [47]

The main benefit of the near-field measurements is that they can be performed in a laboratory environment and in a relatively small space. The biggest downsides are the time consumption of the scanning, which in turn means that a very stable measurement equipment and environment is required due to drifting effects. [51]

7.2. Prototype antennas and the measurement setup

A total of four different lens configurations were produced, 1.0 mm teflon lens, 3.0 mm preperm450 lens, and parallel plate versions of each. Cutting the lenses into shape was performed by water cutting (or water jet cutting), which is a technique used to cut wide variety of materials using extremely high pressure water jets. The main advantages of water cutting are the high accuracy and low operating temperature. Using water alone the method can be used to cut plastics, wood, and other relatively soft materials, and by mixing the water with some abrasive material, e.g., sand, even materials like steel or marble can be cut. Manufactured lenses are presented in Figure 26. Figure 27 shows a photograph of the implemented measurement setup and Figure 28 provides a closer look at the feed – lens interface. [52, 53]
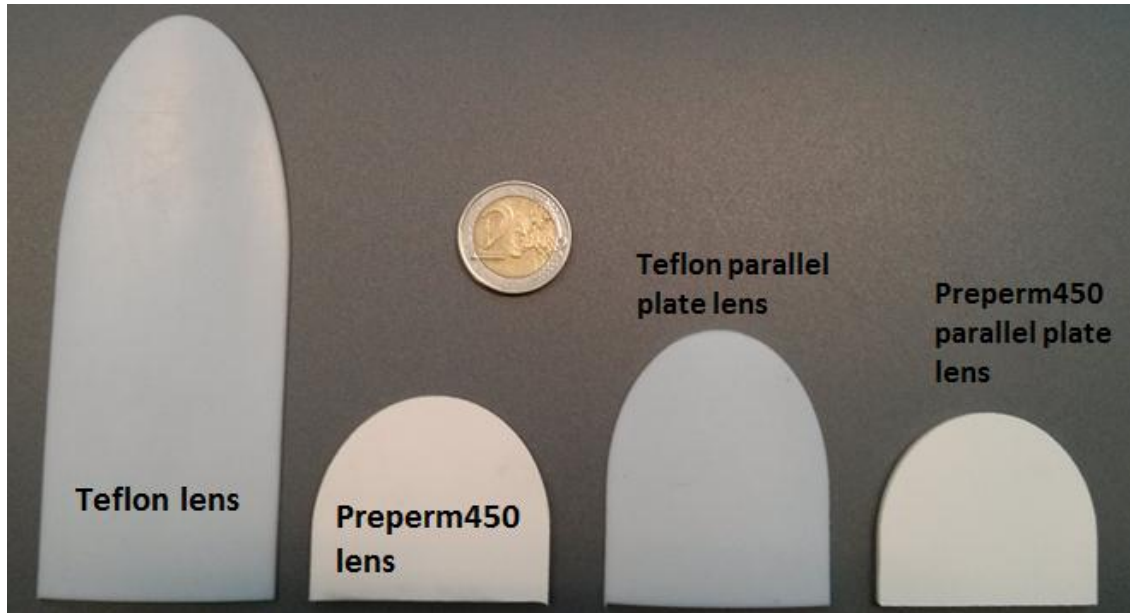
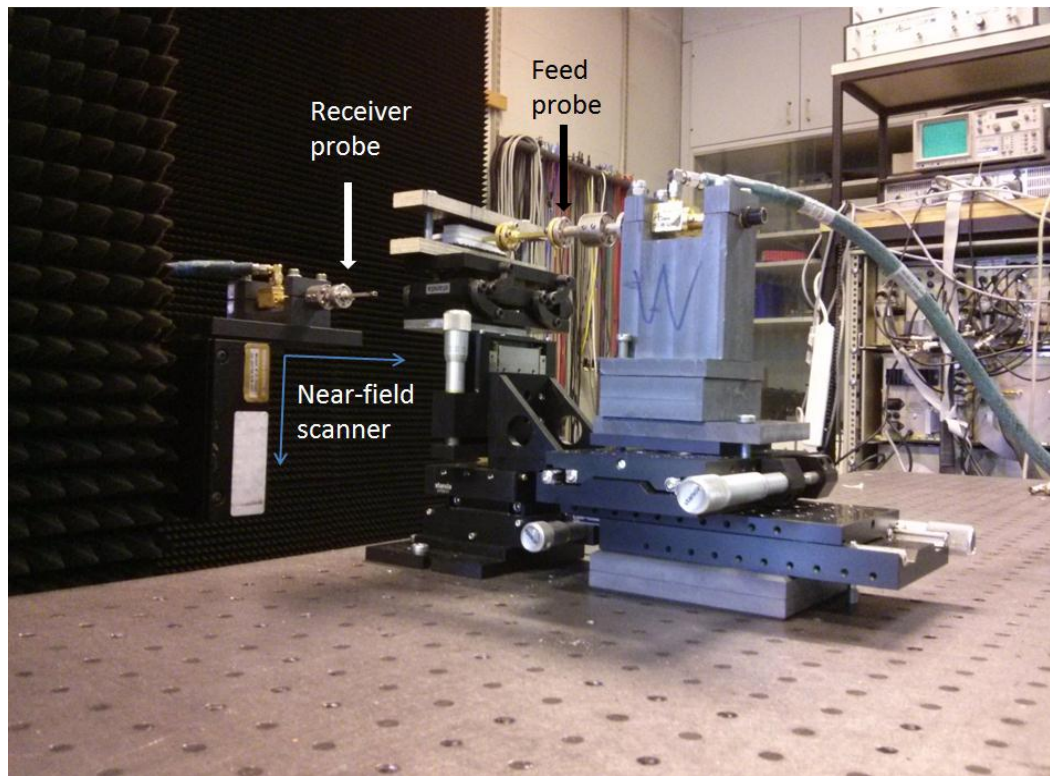Figure 26: Manufactured lens prototypes.

Figure 27: Assembled measurement setup (absorbers removed from the setup for clarity).
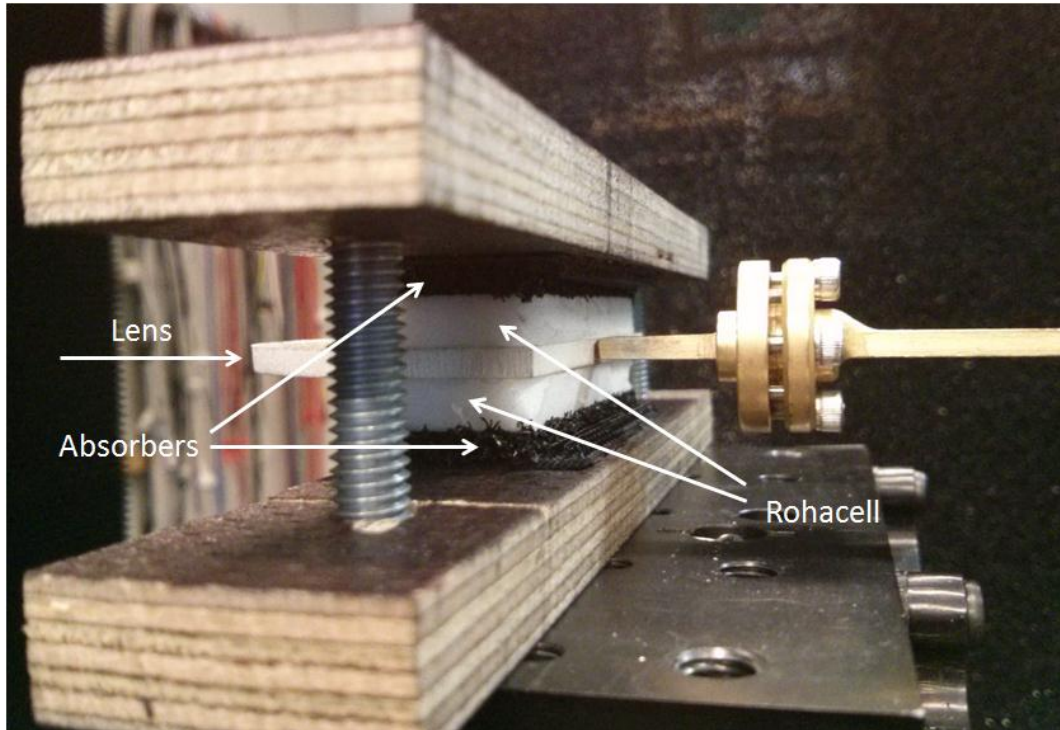
Figure 28: Waveguide feed and preperm450 lens between two sheets of Rohacell51.

The near-field scanner used in the measurements is the model NSI-200V-5x5 by Nearfield Systems Inc. The scanning area of the receiving antenna is 20 cm in x-direction and 30 cm in z-direction (see Figure 11 for reference), and located 21 mm away from the lens. In order to fulfill the Nyquist sampling criterion [28], the sampling interval is set at 2.00 mm ($\approx \frac{1}{2}\lambda_0$) in both directions. The near-field data is analyzed using NSI-2000 computer software, which calculates the far-field of the AUT using the Fourier transform and performs the necessary probe corrections based on the radiation pattern of the WR-10 feed. AB Millimetre MVNA-8-350 millimeter vector network analyzer is used as a measurement device. In order to determine the gain of the AUT, a standard gain horn antenna with known gain is measured and used as a reference value. For each lens, three measurements are conducted using three different feed positions. Additionally, for parallel plate teflon lens one additional measurement is conducted in order to evaluate the level of cross-polarization (XP), i.e., the polarization orthogonal to the reference polarization [4]. The XP measurement is performed by rotating the receiver probe by 90°. Low XP level is an important characteristic of antennas because it enables the implementation of an additional communication channel using orthogonal polarizations at the same frequency band. [54]

8. Results

This chapter presents and discusses the acquired results. The measurement results are compared with the simulation results and the possible reasons for variation between them are analyzed. Section 8.1 focuses on the far-field radiation patterns of the antennas. Section 8.2 discusses the cross-polarization measurement while Section 8.3 concentrates on the beam steering properties of the studied antennas. All results are summarized and discussed further in Section 8.4. All the measurements are conducted at 78.5 GHz.

8.1. Far-field pattern measurements

This section concentrates on the comparison of the simulated and measured far-field patterns of the studied antennas, starting with preperm450 lenses. Figure 29 and Figure 30 show the normalized E- and H-plane radiation patterns of the DSW extended and parallel plate preperm450 lenses.
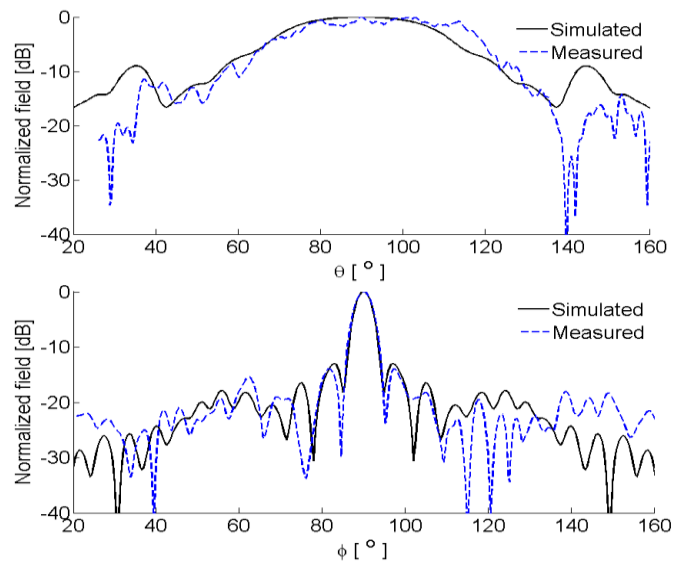

Figure 29: Simulated and measured E- and H-plane patterns of the DSW extended preperm450 lens at 78.5 GHz.
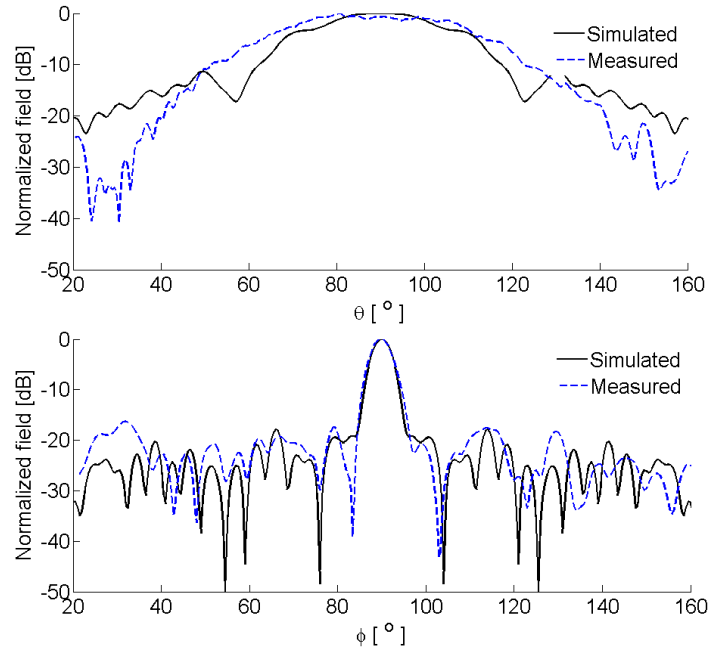
Figure 30: Simulated and measured E- and H-plane patterns of the parallel plate preperm450 lens at 78.5 GHz.

From the figures it can be seen that the measured radiation patterns in both planes correspond relatively well to the simulated radiation patterns. For both lenses, the measured HPBW in E-plane is wider than that of the simulated lens. Larger beamwidth indicates that the effective apertures in *z*-direction are smaller in reality than what is suggested by the simulations. Overall in E-plane the side-lobe levels and the shapes of radiation patterns of the measured lenses correspond well to the simulated ones, and larger differences are noticed only with lowest and highest *Θ*-values, far away from the main beam.

In H-plane for parallel plate lens the shape of the main beam and the first side lobes vary slightly from the simulations. Given the asymmetry of the side lobes, it is possible that the waveguide feed has been slightly misplaced from the center of the lens in the measurement. This would also cause the differences in the positions of the nulls between the simulation and the measurement. Overall, the H-plane patterns of both lens configurations correspond well to the simulations.

Figure 31 and Figure 32 show the E- and H-plane radiation patterns of the measured and simulated teflon lenses.

Figure 31: Simulated and measured E- and H-plane patterns of the DSW extended teflon lens at 78.5 GHz.

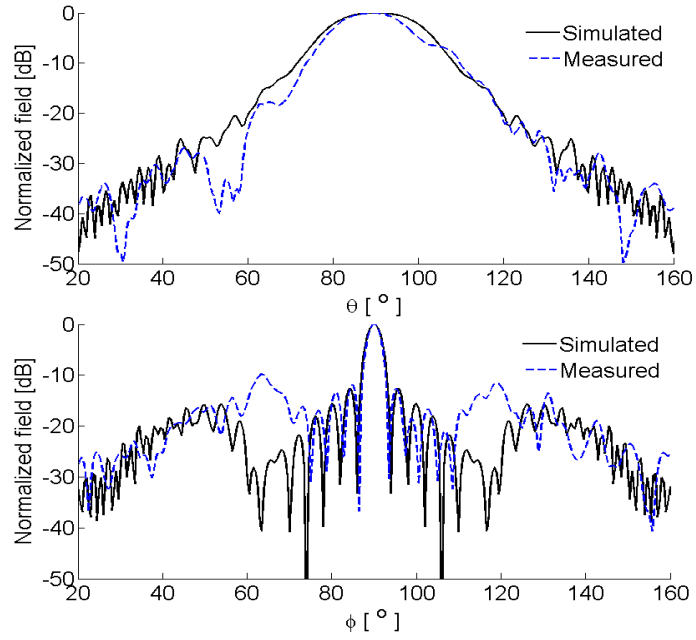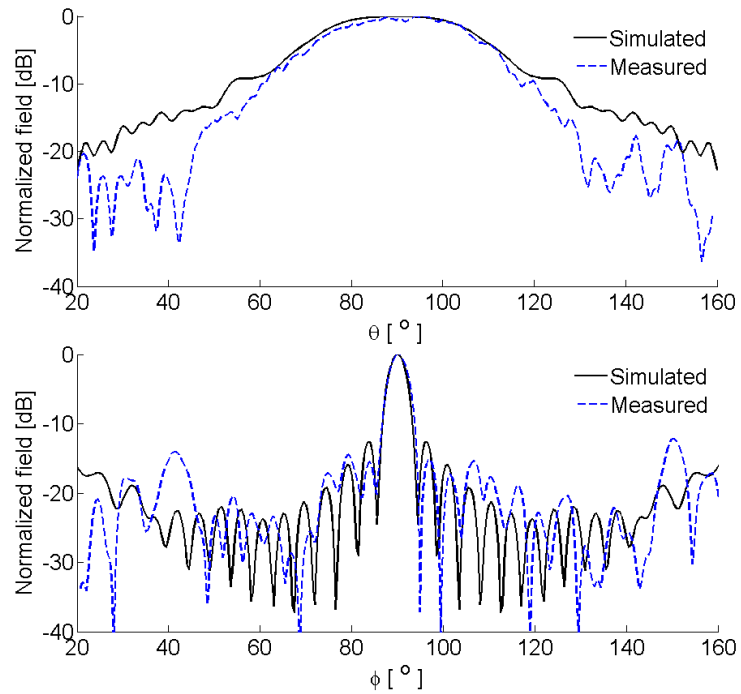Figure 32: Simulated and measured E- and H-plane patterns of the parallel plate teflon lens at 78.5 GHz.

The E-plane pattern of the DSW extended teflon lens is notably asymmetric with respect to $\theta = 90°$ plane. This is a direct consequence of the asymmetry of the prototype lens which is caused by the shape of the teflon sheets from which the lens is manufactured. This causes the lenses to be slightly bent around their axes in *y*-direction (see Figure 33). This effect is not noticed in the E-plane pattern of the parallel plate lens because it is pressed between the metal plates which straighten the lens. No asymmetry is noticed in the H-plane patterns either because the symmetry is maintained in that plane. However, in the H-plane pattern of the DSW lens very high side-lobes are noticed at around $\phi = \pm 30°$ from the center. This is thought to be because of misplaced or inefficient absorbers. Similar behavior can be found from the H-plane pattern without absorbers shown in Figure 12. Overall, the radiation patterns of both lenses correspond well to the simulations around the main beam.

Figure 33: DSW extended teflon lens.

8.1.1. Losses

Comparison between the directivity and gain can be used to evaluate the losses of the antennas as in Section 6.3. Gains of the antennas are determined by measuring a 20 dB standard gain horn antenna for reference, while directivities are calculated directly from the measurement data of each antenna

by the computer software. Simulated and measured losses of all lenses are listed in Table 3, together with the gain and directivity values.

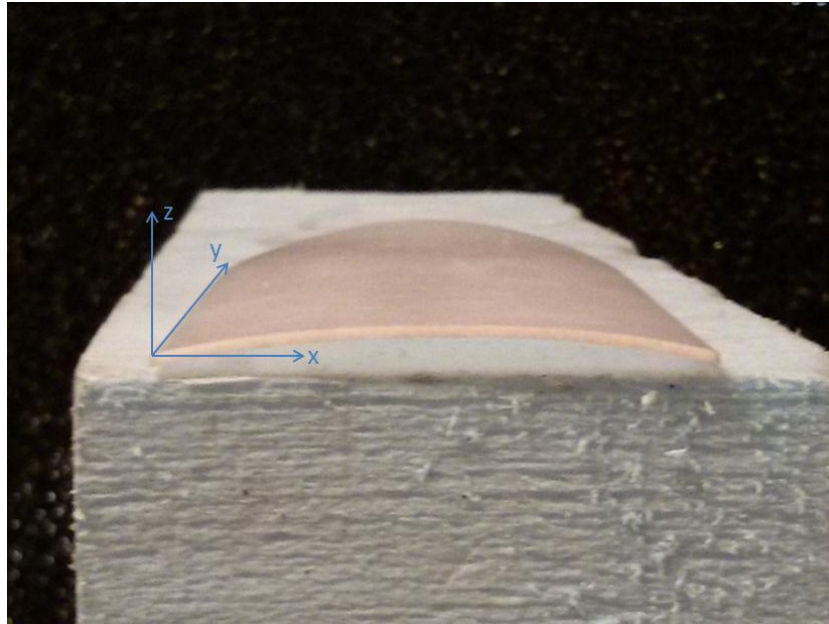Table 3: Simulated and measured directivity, gain, and losses of the studied antennas.

Lens	D [dB]		G [dB]		Loss [dB]	
	Sim.	Meas.	Sim.	Meas.	Sim.	Meas.
DSW extended teflon	24.3	23.9	19.3	17.5	5.0	6.4
Parallel plate teflon	18.7	21.3	18.1	17.1	0.6	4.2
DSW extended preperm450	19.9	20.7	14.6	15.8	5.3	4.9
Parallel plate preperm450	20.6	21.4	12.5	16.1	8.1	5.3

The table shows some significant differences in the losses of both parallel plate lenses. In preperm450 lens the measured losses are significantly lower than in the simulations. This difference is likely caused by uncertainty in the value of the dielectric loss tangent. In [35], where the dielectric properties of preperm450 were measured, the reported measurement uncertainty for dielectric loss tangent was ± 40 %. Figure 24 shows that an error of this magnitude could easily account for the 2.8 dB difference between the simulated and measured losses. The difference is smaller in the DSW extended lens because the waves travel partly in Rohacell. Lower-than-expected dielectric loss tangent also explains the difference between the measured and simulated gains of the preperm450 lenses. The measurement results acquired here would suggest that the dielectric loss tangent of preperm450 is closer to 0.006 than 0.009 reported in [35].

In the parallel plate teflon lens the measured losses are actually more than 4 dB larger than the simulated losses. The most likely cause is thought to be in the matching between the waveguide feed and the lens. In the simulations the reflection coefficient is around -16 dB which is significantly better than in the case of any other lens. It is likely that it is not possible to achieve this good matching in the measurements due to the parallel plates, which increases the losses. Unfortunately this presumption can not be confirmed since the S-parameter measurements are not conducted in this study.

8.2.   Cross-polarization measurement

The measurement of the cross-polarization level of an antenna is realized by rotating the receiving probe by 90° and repeating the original measurement. The XP measurement is conducted only for parallel plate teflon lens but it is indicative of the general cross-polarization properties of flat dielectric lens antennas. Measured and simulated cross-polarization levels are presented in Figure 34.
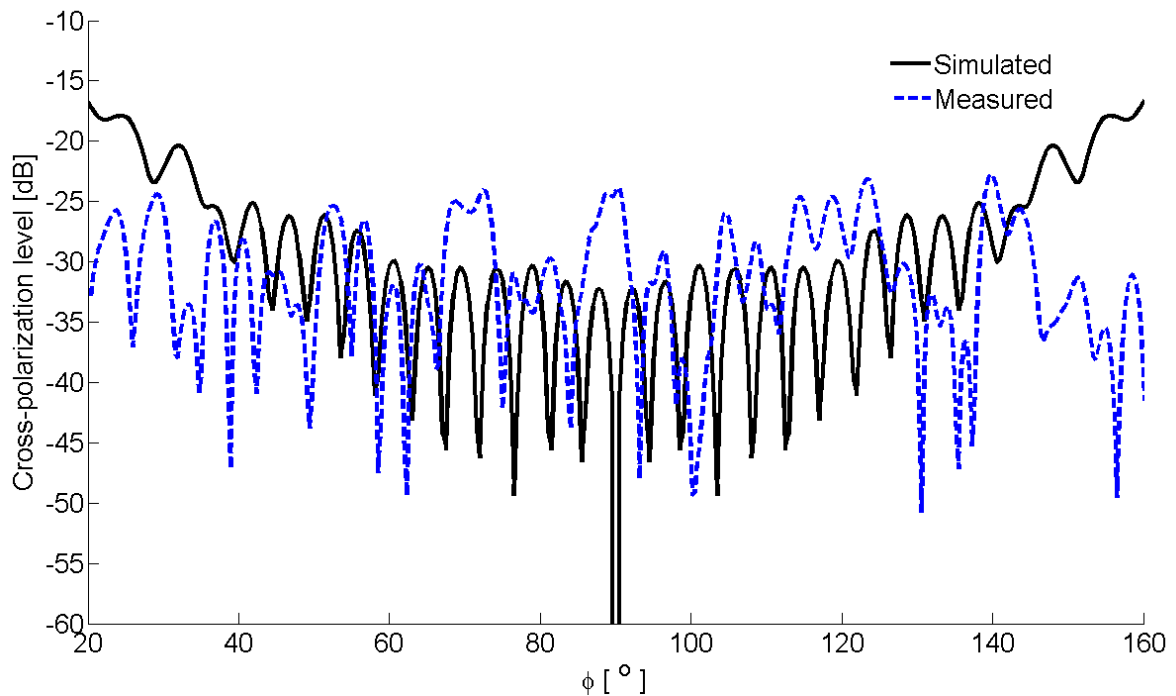
Figure 34: Simulated and measured cross-polarization level of the parallel plate teflon lens at 78.5 GHz.

The figure shows that the simulated and measured cross-polarization levels are very similar. In the simulation the XP level increases with higher values of ϕ while in the measurement the XP level is relatively stable over the whole range. However, around the main lobe at $\phi = 60 - 120°$ the simulated and measured XP levels correspond to each other well, with only some exceptions at around $\theta = 70°$ and $\theta = 90°$. These inconsistencies can be expected to exist due to measurement uncertainty.

8.3.   Beam steering measurements

This section presents the results of the beam steering measurements of all four lenses conducted at 78.5 GHz. Steering of the main beam is realized by changing the position of the waveguide feed. Like discussed earlier, the angle of refraction depends heavily on the effective relative permittivity of the lens. This means that the required feed offset in order to achieve a certain beam steering angle varies from lens to lens. For each lens the aim is to achieve a beam steering angle around 15° and the maximum feed offset is decided based on this goal. However, the effective relative permittivity of the DSW extended teflon lens is so low that an angle of 15° would require an unfeasibly large feed offset. Hence, for this lens configuration the maximum feed offset is decided to be limited at 15.0 mm. In addition to the maximum offsets, one value between 0 mm and the maximum is measured for each lens. Figure 35 illustrates the formation the side lobes and shows how the main beam rotates when the feed point is moved away from the center. [42]
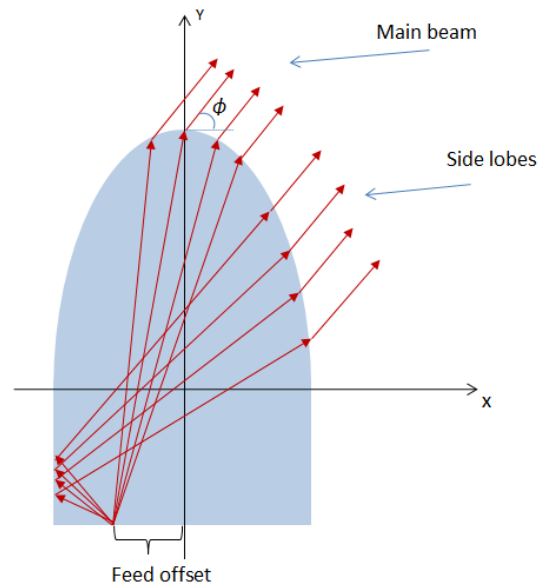
Figure 35: Illustration of the effect of feed offset on the direction of the main beam.

8.3.1. Preperm450 lenses

Figure 36 shows the results of the beam steering measurements and simulations for the preperm450 lenses. The most important simulated and measured results are summarized in Table 4 and Table 5.

Figure 36: Results of the beam steering measurements for preperm450 lenses at 78.5 GHz. a) DSW extended lens and b) Parallel plate lens.

Table 4: Results of the beam steering measurements and simulations of the DSW extended preperm450 lens at 78.5 GHz.

Offset [mm]	D [dB]		G [dB]		Direction of the main beam [$°$]		ϕ_{3dB} [$°$]		FSLL [dB]	
	Sim.	Meas.	Sim.	Meas.	Sim.	Meas.	Sim.	Meas.	Sim.	Meas.
0	19.9	20.7	14.6	15.8	90	90	4.2	4.6	-13.0	-10.8
2.5	19.4	20.8	13.9	15.7	83.0	84.2	4.4	4.7	-9.4	-11.0
5.0	18.4	20.2	12.5	14.9	76.0	76.5	4.9	5.0	-7.2	-8.2

Table 5: Results of the beam steering measurements and simulations of the parallel plate preperm450 lens 78.5 GHz.

Offset [mm]	D [dB]		G [dB]		Direction of the main beam [$°$]		ϕ_{3dB} [$°$]		FSLL [dB]	
	Sim.	Meas.	Sim.	Meas.	Sim.	Meas.	Sim.	Meas.	Sim.	Meas.
0	20.6	21.4	12.5	16.1	90	90	4.4	4.8	-19.4	-17.3
2.5	20.5	21.1	12.0	15.7	82.0	82.0	4.8	5.2	-10.8	-15.7
5.0	18.5	20.7	9.7	14.8	75.0	73.9	5.2	5.9	-7.2	-11.8

The tables show that as the feed offset is increased the simulated gain of both lenses drops more significantly than the measured gain. For the DSW extended lens, in the simulations the gain drop between zero and maximum offsets is 2.1 dB while in the measurements the gain decreases by only 0.9 dB. Similarly, for the parallel plate lens the respective gain drops are 2.8 dB and 1.3 dB. This indicates that the studied lenses are actually more suitable for beam steering than what the simulations suggest.

Slight variation between the simulated and measured beam steering angles is likely explained by the uncertainty in the positioning of the feed. Another possible cause is the varying relative permittivity of preperm450. A ±10 % error in the relative permittivity measurement was reported in [35]. For DSW extended lens the measured beam steering angles are smaller than in the simulations while for parallel plate lens at 5.0 mm offset the angle is 1.1° larger. Because the lenses were manufactured from different material samples, this could indicate that the relative permittivity of the DSW lens is smaller than the one of the parallel plate lens.

The behavior of the SLL is similar in the measurements and the simulations. The measured levels are lower which could mean that in reality more power is transmitted into absorbers and less is reflected inside the lens. HPBWs in H-plane are wider in the measurements of both lenses. This indicates that the effective aperture in *x*-direction is smaller in reality than in the simulations. However, the differences are only around 10 % and the behavior is similar as the feed offset increases. Both these properties, increasing SLL and growing HPBW, are limiting factors when designing the maximum feed offsets.

8.3.2. Teflon lenses

Figure 37 shows the results of the beam steering measurements and simulations for the teflon lenses. The most important simulated and measured results are summarized in Table 6 and Table 7.

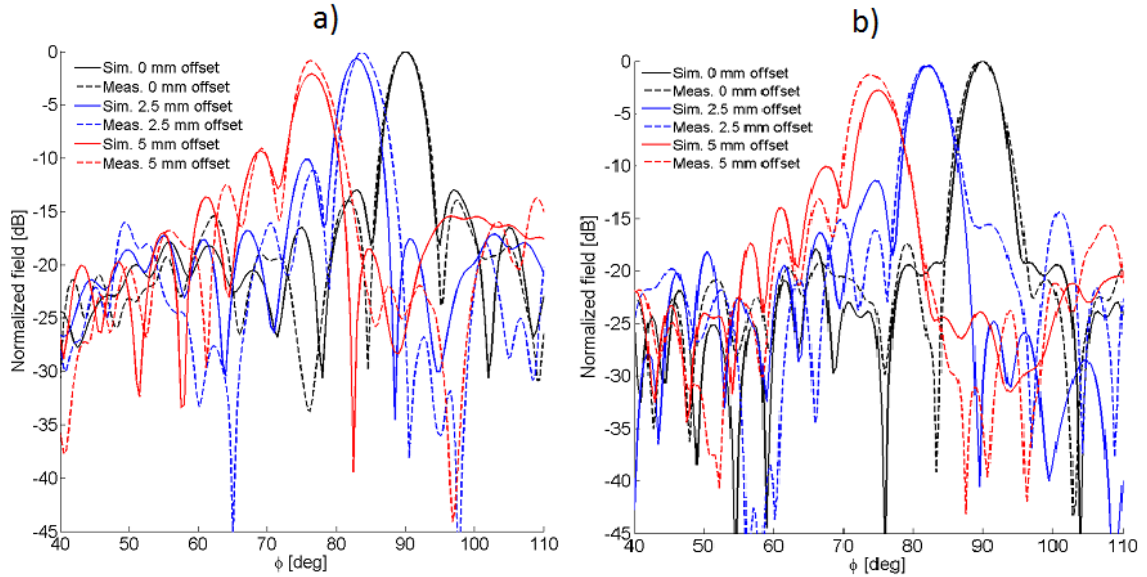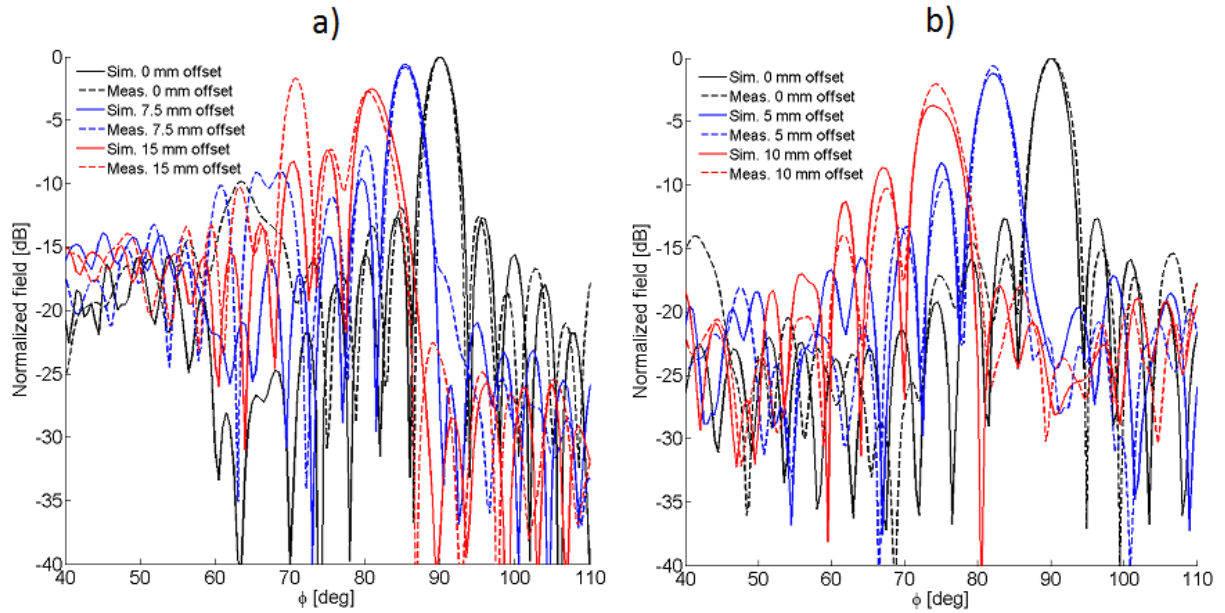Figure 37: Results of the beam-steering measurements for teflon lenses 78.5 GHz. a) DSW extended lens and b) Parallel plate lens.

Table 6: Results of the beam steering measurements and simulations of the DSW extended teflon lens 78.5 GHz.

Offset [mm]	D [dB]		G [dB]		Direction of the main beam [°]		ϕ_{3dB} [°]		FSLL [dB]	
	Sim.	Meas.	Sim.	Meas.	Sim.	Meas.	Sim.	Meas.	Sim.	Meas.
0	24.3	23.9	19.3	17.5	90	90	3.4	2.9	-12.8	-11.9
7.5	23.9	22.8	18.7	16.7	85.5	85.5	3.6	3.4	-9.0	-6.2
15.0	22.3	21.8	16.8	14.7	81.0	80.5	4.3	4.1	-4.8	-4.5

Table 7: Results of the beam steering measurements and simulations of the parallel plate teflon lens 78.5 GHz.

Offset [mm]	D [dB]		G [dB]		Direction of the main beam [°]		ϕ_{3dB} [°]		FSLL [dB]	
	Sim.	Meas.	Sim.	Meas.	Sim.	Meas.	Sim.	Meas.	Sim.	Meas.
0	18.7	21.3	18.1	17.1	90	90	4.1	4.2	-12.7	-15.5
5.0	17.8	21.2	16.9	16.5	82.0	82.0	4.3	3.8	-7.0	-8.9
10.0	15.9	20.8	14.4	15.1	74.0	74.3	5.6	4.7	-4.9	-8.3

The measurement results of the DSW extended lens correspond generally well to the simulation results. The most significant difference is in the SLL, especially with 15 mm offset, which is expected to exist because of the asymmetry of the lens discussed earlier. The decrease in gain and the beam steering angles are almost equal while for the parallel plate lens the gain behaves similarly as in the case of the preperm450 lenses, decreasing less in the measurements than in the simulations.

The behavior of ϕ_{3dB} for parallel plate lens is not as consistent in the measurements as in the simulations, but still in both cases it remains relatively stable when changing the position of the feed from the center to 5 mm offset and increases significantly when increasing the feed offset further to 10 mm. For DSW extended lens at 0 mm offset ϕ_{3dB} is significantly narrower in the measurements but the overall behavior is similar to that of the simulated lens.

8.4.   Summary

This section summarizes the most important findings of the measurements and discusses the overall performance of the prototype antennas in relation to the simulations. Table 8 summarizes the most important properties of the far-field measurements.

Table 8: Summary of the far-field measurement results 78.5 GHz.

Antenna	Gain [dB]		FSLL [dB]		ϕ_{3dB} [°]		θ_{3dB} [°]	
	Sim.	Meas.	Sim.	Meas.	Sim.	Meas.	Sim.	Meas.
DSW ext. preperm450	14.6	15.8	-13.0	-10.8	4.2	4.6	38.6	43.8
Par. plate preperm450	12.5	16.1	-19.4	-17.3	4.4	4.8	28.8	42.2
DSW ext. teflon	19.3	17.5	-12.8	-11.9	3.4	2.9	22.2	17.3
Par. plate teflon	18.1	17.1	-12.7	-15.5	4.1	4.2	35.5	32.2

The measurement and simulation data show that the operation of the prototype antennas is relatively good in comparison with the HFSS simulations. The differences in gain of preperm450 lenses are explained by the lower dielectric loss tangent than what was expected. FSLL of each antenna is within 3 dB of the simulated value which can be considered a good result. Same applies to ϕ_{3dB} values which fall within 0.5° of the simulations. The most interesting measurement result is the θ_{3dB} of the preperm450 parallel plate lens which is almost 50 % wider compared with the simulated value. The reason for this is the presence of the relatively high side-lobes at around ± 30° from the center, which can be noticed in the simulated pattern but not in the measured pattern in Figure 30. It is worth noting that the simulation results would indicate that the insertion of the parallel plates increases the effective aperture in *z*-direction. This means that the measurement result, which suggests that there is effectively no change in the effective aperture, is more sensible.

The most important finding of the beam steering measurements is that, when the feed offset is increased, the gain does not seem to drop as drastically as predicted by the simulations. This is found to be especially true for the preperm450 lenses. Lower gain drop is connected to the side-lobe levels which are lower in most measurements compared with the simulations. This presumption is supported by that fact that the only instances where the measured FSLL is larger than the simulated FSLL (DSW extended teflon lens with 7.5 and 15 mm mm offsets), are also the only measurements where the gain drops more than in the simulations.

A more detailed explanation for why the performance of the measured antennas is so good compared with the simulated antennas would require a thorough investigation of the field and phase distributions inside the lens. This is not possible to be performed within the scope of this thesis.

9. Conclusion

In this Master's thesis, flat dielectric lens antennas and their beam steering properties are studied at millimeter wavelengths. The antenna in question is interesting due to the fan shaped main beam which enables coverage of wide areas using beam steering. This characteristic makes the antenna especially suitable for applications such as automotive radar and wireless communication systems.

Two different lens configurations, a dielectric slab waveguide extended lens and a parallel plate lens, are studied and designed at 78.5 GHz. Both lens types are shaped as extended hemi-ellipses. The design process of the dielectric slab extended lens is relatively complicated due to the surface wave propagation of the waves. This decreases the effective relative permittivity of the dielectric material, which is inversely proportional to the physical dimensions of the lens. The solution for the effective relative permittivity has to be performed numerically which further complicates the design process. In addition, the frequency dependence of the effective relative permittivity limits the use of the lens in broadband applications.

The insertion of the parallel metal plates on both sides of the lens simplifies the antenna structure significantly. For TM polarization, the frequency dependence of the effective relative permittivity almost disappears which allows for more broadband solutions. The physical dimensions of the lens also decrease making the antenna more suitable for portable applications. In addition, the parallel plates shield the lens away from the surrounding increasing the integrability of the antenna.

The lens materials chosen for this study are teflon, which is a common lens material due to its low-loss characteristics and relatively low price, and preperm450 which is a commercial plastic developed especially for high frequency antenna applications. A dielectric slab extended and parallel plate lens prototypes are manufactured from both materials using water jet cutting. The measurements are conducted using a planar near-field scanner and the lenses are fed with a WR-10 open-ended waveguide connected to a vector network analyzer. The measurement results are compared with the simulation results produced with commercial electromagnetic simulation software.

The measurement results show that, to a large extent, the behavior of the antennas is consistent with the computer simulations. The most significant differences are found in losses of the antennas, which are explained by the uncertainty in the dielectric properties of the materials. Some variation is also noticed in the beam widths and side-lobe levels of the antennas, but generally the correlation between the simulated and measured results is high. In a few measurements some notable asymmetry in the radiation patterns is found. Most probable causes for these findings are the asymmetry of the teflon lenses and small errors in the positioning of the waveguide feed. The cross-polarization level of one of the lenses is measured as well and found to be very low and consistent with the simulation results.

The objective of the beam steering measurement is to produce a beam steering angles of around 15°. However, using a dielectric slab waveguide extended teflon lens this is not feasible due to the low effective index of refraction of the lens, and the largest achieved beam steering angle is below 10°. The results of the beam steering measurement show that in several cases, as the main beam is steered, the prototype lenses perform even better than the simulated lenses, showing higher gain levels and lower side-lobe levels relative to the gain of the on-axis fed lens. Slight variation in the beam steering angles is noticed but it can be explained by varying relative permittivity of the preperm450 material samples and by errors in the feed positioning.

The acquired results confirm the suitability of flat dielectric lens antennas for beam steering applications at millimeter wavelengths. Furthermore, preperm450 is found to be an excellent material choice for dielectric lens antennas at millimeter wave frequencies.

The next natural step towards real-life applications would be to replace the open-ended waveguide feed with an antenna array. Future work on this topic could also include an expansion of the study from a single frequency to a larger frequency band in order to study the broadband properties of the flat dielectric lens antennas, and studying the possibilities to reduce the internal reflections by shaping the extension part of the lens differently.

References

[1]   X. Wu, G. V. Eleftheriades, and E. Van Deventer-Perkins, "Design and characterization of single and multiple beam mm-wave circularly polarized substrate lens antennas for wireless communications," in *IEEE Antennas and Propagation Society International Symposium*, Orlando, Florida, 11-16 July 1999, vol. 4, pp. 2408-2411.

[2]   A. Boriskin, R. Sauleau, and A. Nosich, "2-D Analysis of synthesis of dielectric lens antennas with boundary integral equations," in *Microwaves, Radar and Remote Sensing Symposium MRRS-2008*, Kiev, Ukraine, 22-24 September 2008, pp. 196-200.

[3]   J. Costa, E. Lima, and C. Fernandez, "Compact beam-steerable lens antenna for 60-GHz wireless communications," *IEEE Transactions on Antennas and Propagation,* vol. 57, no. 10, pp. 2926-2933, October 2009.

[4]   Antenna Standards Committee of the IEEE Antennas and Propagation Society, "IEEE standard definitions of terms for antennas," *IEEE Std 145-1993,* p. 40, April 1993.

[5]   Z. Chen, J. Liu, and L. Li, "Design of scalable beam steering system of phased array radar," in *IEEE CIE International Conference on Radar*, Chengdu, China, 24-27 October 2011, vol. 2, pp. 1153-1156.

[6]   H. H. G. Hansen, R. G. P. Lopata, T. Idzenga, and C. De Korte, "High quality non-invasive full 2D strain tensor imaging using a beam steered linear array ultrasound transducer," in *IEEE International Ultrasonics Symposium (IUS)*, Rome, Italy, 20-23 September 2009, pp. 159-162.

[7]   C. Reardon, A. Di Falco, K. Welna, and T. Krauss, "Optical beam-steering for wireless sensor networks," in *LEOS Annual Meeting Conference Proceedings*, Belek-Antalya, Turkey, 4-8 October 2009, pp. 583-583.

[8]   M. Kyrö, D. Titz, V. Kolmonen, S. Ranvier, P. Pons, C. Luxey, and P. Vainikainen, "5 x 1 linear antenna array for 60 GHz beam steering applications," in *Proceedings of the 5th European Conference on Antennas and Propagation (EUCAP)*, Rome, Italy, 11-15 April 2011.

[9]   Y. Monnai, V. Viereck, H. Hillmer, K. Altmann, C. Jansen, M. Koch, and H. Shinoda, "Terahertz beam steering using structured MEMS surfaces for networked wireless sensing," in *Ninth International Conference on Networked Sensing Systems (INSS)*, Antwerp, Belgium, 11-14 June 2012.

[10] J. Ala-Laurinaho, A. Karttunen, J. Säily, A. Lamminen, R. Sauleau, and A. Räisänen, "MM-wave lens antenna with an integrated LTCC feed array for beam steering," in *Proceedings of the fourth European conference on antennas and propagation (EUCAP)*, Barcelona, Spain, 12-16 April 2010.

[11] B. Schoenlinner, X. Wu, J. P. Ebling, G. V. Eleftheriades, and G. M. Rebeiz, "Wide-scan spherical-lens antennas for automotive radars," *IEEE Transactions on Microwave Theory and Techniques,* vol. 50, no. 9, pp. 2166-2175, 2002.

[12] T. Komljenovic and Z. Sipus, "Dielectric lens antennas design at millimeter waves," in *ELMAR, 2008. 50th International Symposium*, Zadar, Croatia, 10-12 September 2008, pp. 621-624.

[13] Computer Simulation Technology (CST), "A dielectric lens antenna with enhanced aperture efficiency for industrial radar applications," May 2011. [Online]. Available: http://www.cst.com/Content/Applications/Article/A+Dielectric+Lens+Antenna+with+Enhanced+Aperture+Efficiency+for+Industrial+Radar+Applications. [Accessed July 2013].

[14] C. Balanis, *Antenna Theory: Analysis and Design*, New York, Harper & Row, 1st ed., 1982, 790p.

[15] J. Qiu, W. Li, and Y. Suo, "A Novel high gain beam scanning hemispherical dielectric lens antenna," in *6th International Conference on ITS Telecommunications*, Chengdu, China, 21-23 June 2006.

[16] T. K. Nguyen, I. Woo, H. Han, I. Park, and H. Lim, "Four-leaf clover-shaped antenna on an extended hemishperical lens for a high-output-power THz photomixer," in *35th International Conference on Infrared Millimeter and Terahertz Waves (IRMMW-THz)*, Rome, Italy, 5-10 September 2010.

[17] A. Weily and N. Nikolic, "Dual-polarized planar feed for low-profile hemispherical Luneburg lens antennas," *IEEE Transactions on Antennas and Propagation,* vol. 60, no. 1, pp. 402-407, September 2012.

[18] C. Schulz, C. Baer, N. Pohl, T. Musch, and I. Rolfes, "A Multistatic feeding concept for beam steering based on a dielectric ellipsoidal antenna," in *Asia-Pacific Microwave Conference Proceedings (APMC)*, Kaohsiung, Taiwan, 4-7 December 2012.

[19] S. Baev, S. Gechev, B. Hadjistamov, and P. Dankov, "Modeling and Simulations of Lüneburg Lens Antennas for Communication Purposes," in *16th Telecommunications Forum TELFOR2008*, Belgrade, Serbia, 25-27 November 2008.

[20] H. Mosallaei and Y. Rahmat-Samii, "Nonuniform Luneburg and two-shell lens antennas: Radiation characteristics and design optimization," *IEEE Transactions on Antennas and Propagation,* vol. 49, no. 1, pp. 60-69, January 2001.

[21] A. Rolland, R. Sauleau, and M. Drissi, "Design of H-plane shaped flat lenses using a 2-D approach based on FDTD and genetic algorithm," in *Proceedings of the Fourth European Conference on Antennas and Propagation (EuCAP)*, Barcelona, Spain, 12-16 April 2010.

[22] A. Rolland, R. Sauleau, and L. Le Coq, "Flat shaped dielectric lens antenna for 60-GHz applications," *IEEE Transactions on Antennas and Propagation,* vol. 59, no. 11, pp. 4041-4048, August 2010.

[23] B. Chantraine-Bares, R. Sauleau, L. Le Coq, and K. Mahdjoubi, "A new accurate design method for millimeter-wave homogeneous dielectric substrate lens antennas of arbitrary shape," *IEEE Transactions on Antennas and Propagation,* vol. 53, pp. 1069-1082, March 2005.

[24] B. Fuchs, R. Golubovic, A. K. Skriverick, and J. R. Mosig, "Spherical lens antenna designs with particle swarm optimization," *Microwave and Optical Technology Letters,* vol. 52, no. 7, pp. 1655-1659, April 2010.

[25] L. Xue and V. Fusco, "Patch fed planar dielectric slab extended hemi-elliptical lens antenna," *IEEE Transactions of Antennas and Propagation,* vol. 56, no. 3, pp. 661-666, March 2008.

[26] L. Xue and V. Fusco, "Polarisation insensitive planar dielectric slab waveguide extended hemi-elliptical lens," *IET Microwaves, Antennas & Propagation,* vol. 2, no. 4, pp. 312-315, June 2008.

[27] J. E. Midwinter, *Optical Fibres for Transmission*, New York, John Wiley & Sons, 1979, 410p.

[28] H. Young and R. Freedman, *University Physics with Modern Physics with Mastering Physics*, San Francisco, Pearson & Addison Wesley, 11th ed., 2003, 1714p.

[29] R. E. Collin, *Foundations for Microwave Engineering*, New York, McGraw-Hill, 2nd ed., 1966, 950p.

[30] F. E. Gardiol, *Introduction to Microwaves*, Massachusetts, Artech House, Inc., 1984, 495p.

[31] I. Lindell, *Aaltojohtoteoria*, Espoo, Otatieto, 1997, 345p.

[32] J. F. Lotspeich, "Explicit general eigenvalue solutions for dielectric slab waveguides," *Applied Optics,* vol. 14, no. 2, 1975.

[33] R. A. Adams, *Calculus: A Complete Course*, Toronto, Addison Wesley Longman, 5th ed., 2003, 999p.

[34] Premix, "Preperm® L450 technical datasheet," October 2012. [Online]. Available: http://www.premixgroup.com/wordpress/wp-content/files_mf/preperm_l450_tds.pdf. [Accessed July 2013].

[35] K. Piiroinen, *Determination of Dielectric Properties Using a Vector Network Analyzer*, Special assignment, Aalto University School of Electrical Engineering, Espoo, October 2012.

[36] Ansys Inc., *HFSS v14.0 Material library.*

[37] Antenna Standards Committee of the IEEE Antennas and Propagation Society, "IEEE standard test procedures for antennas," *ANSI/IEEE Std 149-1979,* p. 135, December 1979.

[38] Evonik Industries, [Online]. Available: http://www.rohacell.com/product/rohacell/en/products-services/pages/default.aspx. [Accessed June 2013].

[39] D. Bourreau, A. Péden, and S. Le Maguer, "A quasi-optical free-space measurement setup without time-domain gating for material characterization in the W-band," *IEEE Transactions on Instrumentation and Measurement,* vol. 55, no. 6, pp. 2022-2028, December 2006.

[40] High Frequency Structure Simulator (HFSS), v.14.0, [Online]. Available: www.ansys.com. [Accessed June 2013].

[41] Ansys Inc., *HFSS v14 User's manual: Technical details on finite element method.*

[42] A. Karttunen, J. Ala-Laurinaho, R. Sauleau, and A. V. Räisänen, "Reduction of internal reflections in integrated lens antennas for beam-steering," *Progress in Electromagnetics Research,* vol. 134, pp. 63-78, 2013.

[43] L. Felsen, F. Akleman, and L. Sevgi, "Wave propagation inside a two-dimensional perfectly conducting parallel-plate waveguide: hybrid ray-mode techniques and their visualizations," *IEEE Antennas and Propagation Magazine,* vol. 46, no. 6, pp. 69-89, December 2004.

[44] J. A. Higgins, *Measurement and simulation of parallel plate waveguide structures in the terahertz region for sensing and material characterization applications*, Master's thesis, Portland State University, Oregon, 2012.

[45] K. Rasilainen, *Antenna Performance in Bendable Mobile Devices*, Master's thesis, Aalto University School of Electrical Engineering, Espoo, 2012.

[46] G. Djuknic, "Method of measuring a pattern of electromagnetic radiation", USA Patent US 20030142023 A1, January 2002.

[47] A. Yaghjian, "An overview of near-field antenna measurements," *IEEE Transactions on Antennas and Propagation,* vol. 34, no. 1, pp. 30-45, January 1986.

[48] University of Stuttgart, "Near-field antenna measurements," March 2006. [Online]. Available: www.ihf.uni-stuttgart.de/forschung/forschungsgebiete/nahfeld/index.html. [Accessed June 2013].

[49] C. Parini and M. Philippakis, "Compact antenna test range reflector edge treatment," *Electronics Letters,* vol. 32, no. 2, pp. 82-83, January 1996.

[50] J. Ala-Laurinaho, J. Häkli, A. Karttunen, T. Koskinen, A. Lonnqvist, J. Mallat, E. Noponen, A. Tamminen, M. Vaaja, V. Viikari, A. Räisänen, and J. Lemanczyk, "Tests of 1.5-m Reflector Antenna in a 650 GHz Hologram CATR," in *The Second European Conference on Antennas and Propagation (EuCAP)*, Edinburgh, Scotland, 11-16 November 2007.

[51] D. Janse van Rensburg and G. Hindman, "An overview of near-field sub-millimeter wave antenna test applications," in *14th Conference on microwave techniques, COMITE 2008*, Prague, Czech Republic, 23-24 April 2008.

[52] WaterJets.org, "About water jets," 2013. [Online]. Available: http://waterjets.org/index.php?option=com_content&task=category&sectionid=4&id=46&Itemid=53. [Accessed August 2013].

[53] B. G. Schwacha, "Liquid cutting of hard materials", USA Patent 2985050, May 1961.

[54] A. C. Ludwig, "The definition of cross polarization," *IEEE Transaction on Antennas and Propagation,* vol. 21, no. 1, pp. 116-119, January 1973.